Robust efficiency and actuator saturation explain healthy heart rate control and variability

Na Li[a], Jerry Cruz[b], Chenghao Simon Chien[c,d], Somayeh Sojoudi[e], Benjamin Recht[f], David Stone[g], Marie Csete[h], Daniel Bahmiller[b], and John C. Doyle[b,c,i,1]

[a]School of Engineering and Applied Sciences, Harvard University, Cambridge, MA 02138; [b]Department of Computing and Mathematical Science, California Institute of Technology, Pasadena, CA 91125; [c]Department of Electrical Engineering, California Institute of Technology, Pasadena, CA 91125; [d]Advanced Algorithm Research Center, Philips Healthcare, Thousand Oaks, CA 91320; [e]Department of Neurology, New York University Comprehensive Epilepsy Center, New York University School of Medicine, New York, NY 10016; [f]Department of Electrical Engineering and Computer Sciences and Department of Statistics, University of California, Berkeley, CA 94720; [g]Departments of Anesthesiology and Neurosurgery and the Center for Wireless Health, University of Virginia School of Medicine, Charlottesville, VA 22908; [h]Huntington Medical Research Institutes, Pasadena, CA 91101; and [i]Department of BioEngineering, California Institute of Technology, Pasadena, CA 91125

Edited* by Michael S. Gazzaniga, University of California, Santa Barbara, CA, and approved June 27, 2014 (received for review January 30, 2014)

The correlation of healthy states with heart rate variability (HRV) using time series analyses is well documented. Whereas these studies note the accepted proximal role of autonomic nervous system balance in HRV patterns, the responsible deeper physiological, clinically relevant mechanisms have not been fully explained. Using mathematical tools from control theory, we combine mechanistic models of basic physiology with experimental exercise data from healthy human subjects to explain causal relationships among states of stress vs. health, HR control, and HRV, and more importantly, the physiologic requirements and constraints underlying these relationships. Nonlinear dynamics play an important explanatory role—most fundamentally in the actuator saturations arising from unavoidable tradeoffs in robust homeostasis and metabolic efficiency. These results are grounded in domain-specific mechanisms, tradeoffs, and constraints, but they also illustrate important, universal properties of complex systems. We show that the study of complex biological phenomena like HRV requires a framework which facilitates inclusion of diverse domain specifics (e.g., due to physiology, evolution, and measurement technology) in addition to general theories of efficiency, robustness, feedback, dynamics, and supporting mathematical tools.

system identification | optimal control | respiratory sinus arrhythmia

Biological systems display a variety of well-known rhythms in physiological signals (1–6), with particular patterns of variability associated with a healthy state (2–6). Decades of research demonstrate that heart rate (HR) in healthy humans has high variability, and loss of this high HR variability (HRV) is correlated with adverse states such as stress, fatigue, physiologic senescence, or disease (6–13). The dominant approach to analysis of HRV has been to focus on statistics and patterns in HR time series that have been interpreted as fractal, chaotic, scale-free, critical, etc. (6–17). The appeal of time series analysis is understandable as it puts HRV in the context of a broad and popular approach to complex systems (5, 18), all while requiring minimal attention to domain-specific (e.g., physiological) details. However, despite intense research activity in this area, there is limited consensus regarding causation or mechanism and minimal clinical application of the observed phenomena (10). This paper takes a completely different approach, aiming for more fundamental rigor (19–24) and methods that have the potential for clinical relevance. Here we use and model data from experimental studies of exercising healthy athletes, to add simple physiological explanations for the largest source of HRV and its changes during exercise. We also present methods that can be used to systematically pursue further explanations about HRV that can generalize to less healthy subjects.

Fig. 1 shows the type of HR data analyzed, collected from healthy young athletes ($n = 5$). The data display responses to changes in muscle work rate on a stationary bicycle during mostly aerobic exercise. Fig. 1*A* shows three separate exercise sessions with identical workload fluctuations about three different means. With proper sleep, hydration, nutrition, and prevention from overheating, trained athletes can maintain the highest workload in Fig. 1 for hours and the lower and middle levels almost indefinitely. This ability requires robust efficiency: High workloads are sustained while robustly maintaining metabolic homeostasis, a particularly challenging goal in the case of the relatively large, metabolically demanding, and fragile human brain.

Whereas mean HR in Fig. 1*A* increases monotonically with workloads, both slow and fast fluctuations (i.e., HRV) in HR are saturating nonlinear functions of workloads, meaning that both high- and low-frequency HRV component goes down. Results from all subjects showed qualitatively similar nonlinearities (*SI Appendix*). We will argue that this saturating nonlinearity is the simplest and most fundamental example of change in HRV in response to stressors (11, 12, 25) [exercise in the experimental case, but in general also fatigue, dehydration, trauma, infection, even fear and anxiety (6–9, 11, 12, 25)].

Physiologists have correlated HRV and autonomic tone (7, 11, 12, 14), and the (im)balance between sympathetic stimulation and parasympathetic withdrawal (12, 26–28). The alternation in autonomic control of HR (more sympathetic and less parasympathetic tone during exercise) serves as an obvious proximate cause for how the HRV changes as shown in Fig. 1, but the ultimate question remains as to why the system is implemented

Significance

Reduction in human heart rate variability (HRV) is recognized in both clinical and athletic domains as a marker for stress or disease, but previous mathematical and clinical analyses have not fully explained the physiological mechanisms of the variability. Our analysis of HRV using the tools of control mathematics reveals that the occurrence and magnitude of observed HRV is an inevitable outcome of a controlled system with known physiological constraints. In addition to a deeper understanding of physiology, control analysis may lead to the development of timelier monitors that detect control system dysfunction, and more informative monitors that can associate HRV with specific underlying physiological causes.

Author contributions: N.L., J.C., B.R., and J.C.D. designed research; N.L., J.C., C.S.C., B.R., D.B., and J.C.D. performed research; N.L., J.C., S.S., B.R., and J.C.D. contributed new reagents/analytic tools; N.L., J.C., C.S.C., S.S., and J.C.D. analyzed data; and N.L., D.S., M.C., and J.C.D. wrote the paper.

The authors declare no conflict of interest.

*This Direct Submission article had a prearranged editor.

[1]To whom correspondence should be addressed. Email: doyle@caltech.edu.

This article contains supporting information online at www.pnas.org/lookup/suppl/doi:10.1073/pnas.1401883111/-/DCSupplemental.

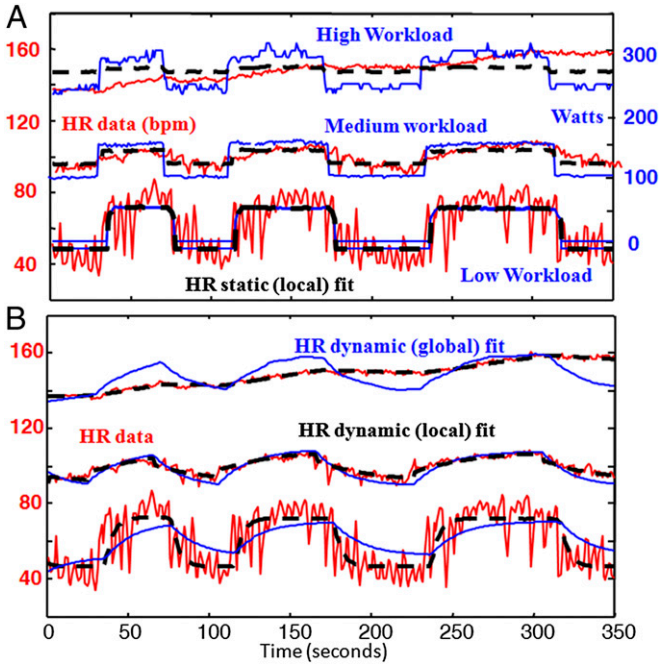

Fig. 1. HR responses to simple changes in muscle work rate on a stationary bicycle: Each experimental subject performed separate stationary cycle exercises of ~10 min for each workload profile, with different means but nearly identical square wave fluctuations around the mean. A typical result is shown from subject 1 for three workload profiles with time on the horizontal axis (zoomed in to focus on a 6-min window). (*A*) HR (red) and workload (blue); linear local piecewise static fits (black) with different parameters for each exercise. The workload units (most strenuous exercise on top of graph) are shifted and scaled so that the blue curves are also the best global linear fit. (*B*) Corresponding dynamics fits, either local piecewise linear (black) or global linear (blue). Note that, on all time scales, mean HR increases and variability (HRV) goes down with the increasing workload. Breathing was spontaneous (not controlled).

this way. It could be an evolutionary accident, or could follow from hard physiologic tradeoff requirements on cardiovascular control, as work in other systems suggests (1). Here, the explanation of HRV similarly involves hard physiological tradeoffs in robust efficiency and employs the mathematical tools necessary to make this explanation rigorous in the context of large measurement and modeling uncertainties.

Physiological Tradeoffs

The central physiological tradeoffs in cardiovascular control (27–32), shown schematically in Fig. 2, involve interconnected organ systems and four types of signals that are very different in both functional role and time series behavior, but together define the requirements for robust efficiency of the cardiorespiratory system. The main control requirement is to maintain (*i*) small, acceptable "errors" in internal variables for brain homeostasis [e.g., cerebral blood flow (CBF), arterial O_2 saturation (SaO_2)] and efficient working muscle O_2 utilization (ΔO_2) using (*ii*) actuators (heart rate H, minute ventilation $\dot{V}_E$, vasodilation and systemic peripheral resistance R_s, and brain autoregulation) in response to (*iii*) external disturbances (workload W), and (*iv*) internal sensor noise and perturbations (e.g., pressure changes from different respiratory patterns due to pulsatile ventilation V).

In healthy fit subjects, keeping errors in CBF, SaO_2, and ΔO_2 suitably small while responding to large, fast variations in W disturbance necessitates compensating and coordinated changes in actuation via responses in H, $\dot{V}_E$, R_s, and cerebral autoregulation. Thus, healthy response involves low error but high control variability whereas loss of health is exactly the opposite. We will show that the observed striking changes in HRV such as those seen in Fig. 1 result from tradeoffs between these errors combined with various actuator saturations.

A challenge to this approach lies in managing the necessary but potentially bewildering complexity inherent in the physiological details, mathematical methods, and measurement technology. To achieve this, we make each small step in the analysis as simple, accessible, and reproducible as possible from analysis of experimental data to modeling to physiological and control theoretic interpretation. In addition, we restrict the physiology (shown schematically in Fig. 2) (27–32) and control theory (32–35) to basic levels and all software is standard and open source. We also make several passes through the analysis and modeling with increasing complexity, sophistication, and depth, to aid intuition while highlighting the need for rigorous, scalable methods.

In addition to mechanistic physiological models, we also use systems identification techniques (referred to as "black-box" fits in this paper) (25, 33, 36, 37) as intermediate steps to identify parsimonious canonical dynamical input–output models relating HR as an output variable to input disturbances such as workload and ventilation. These techniques establish causal deterministic links between input and output variables, highlight the aspects of time series and dynamic relationships that are explored further, and give some indication of the degree of complexity of their dynamics. Then, we use physiologically motivated models (referred to as "first-principle" models in this paper) (29–32) to study the mechanisms that drive the dynamics. The two approaches are complementary: Black-box fits highlight essential relationships that may be hard to intuit from data alone and can be obscured in both complex data sets and mechanistic models,

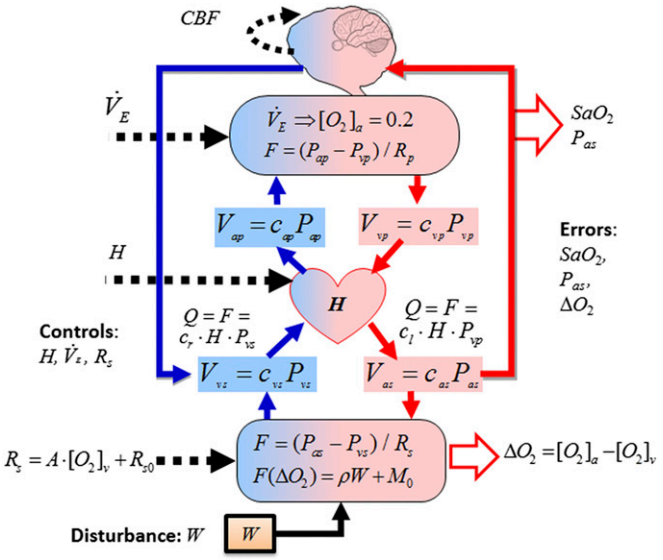

Fig. 2. Schematic for cardiovascular control of aerobic metabolism and summary of main variables: Blue arrows represent venous beds, red arrows are arterial beds, and dashed lines represent controls. Four types of signals, distinct in both functional role and time series behavior, together define the required elements for robust efficiency. The main control requirement is to maintain (*i*) small errors in internal variables for brain homeostasis (e.g., arterial O_2 saturation SaO_2, mean arterial blood pressure P_{as}, and CBF), and muscle efficiency (oxygen extraction ΔO_2 across working muscle) despite (*ii*) external disturbances (muscle work rate W), and (*iii*) internal sensor noise and perturbations (e.g., pressure changes from different respiratory patterns due to pulsatile ventilation V) using (*iv*) actuators (heart rate H, minute ventilation V_E, vasodilatation and peripheral resistance R, and local cerebral autoregulation).

whereas first-principles models give physiological interpretations to these dynamical relationships.

Results

Static Fits. Table 1 lists the minimum root-mean-square (rms) error $||H\_data\text{-}H\_fit||$ (where $\|x\| = \sqrt{\sum_{t=1}^{N}(x_t)^2/N}$ for a time series x_t of length N) for several static and dynamic fits of increasing complexity for the data in Fig. 1. Not surprisingly, Table 1 shows that the rms error becomes roughly smaller with increased fit complexity (in terms of the number of parameters). Rows 2 and 5 of Table 1 are single global linear fits for all of the data, whereas the remaining rows have different parameters for each cell and are thus piecewise linear when applied to all of the data. The "best" piecewise linear models balancing error with complexity are further highlighted in yellow in Table 1.

We will initially focus on static linear fits (first four rows) of the form $h(W) = b{\cdot}W + c$, where b and c are constants that minimize the rms error $||H\_data\text{-}h(W)||$, which can be found easily by linear least squares. Static models have limited explanatory power but are simple starting points in which constraints and tradeoffs can be easily identified and understood, and we use only methods that directly generalize to dynamic models (shown later) with modest increase in complexity. Row 1 of Table 1 is the trivial "zero" fit with $b = c = 0$; row 2 is the best global linear fit with $(b,c) = (0.35,53)$ which is used to linearly scale the units of W (blue) to best fit the HR data (red) in Fig. 1*A*; row 3 is a piecewise constant fit with $b = 0$ and c being the mean of each data set; row 4 is the best piecewise linear fits (black dashed lines in Fig. 1*A*) with quite different values (b,c) of (0.44,49), (0.14,82), and (0.04,137) at 0–50, 100–150, and 250–300 W. The piecewise linear model in row 4 has less error than the global linear fit in row 2. At high workload level, HR in Fig. 1 does not reach steady state on the time scale of the experiments, the linear static fit is little better than constant fit, and so these data are not considered further for static fits and models.

Both Table 1 and Fig. 1 imply that HR responds somewhat nonlinearly to different levels of workload stressors. The solid black curve in Fig. 3*A* shows idealized (i.e., piecewise linear) and qualitative but typical values for $h(W)$ globally that are consistent with the static piecewise linear fits at the two lower watts levels in Fig. 1*A*. The change in slope of $H = h(W)$ with increasing workload is the simplest manifestation of changing HRV and is now our initial focus. A proximate cause is autonomic nervous system balance, but we are looking for a deeper "why" in terms of whole system constraints and tradeoffs.

Static Models. As we mentioned earlier, in healthy fit subjects, the central physiological tradeoffs in cardiovascular control require keeping errors such as CBF, SaO_2, and ΔO_2 suitably small in response to variations in W disturbance through changes in actuations such as H. To better understand the tradeoff, we derive a steady-state model $(P_{as}, \Delta O_2) = f(H, W)$ from standard physiology that constrains the relationship between $(P_{as}, \Delta O_2)$ and (H, W) independent of how H is controlled (details below). Here P_{as} is mean systemic arterial blood pressure, which is an important variable affecting the CBF (28, 38) and ΔO_2 is the drop in oxygen content across working muscle [Notice that the model already assumes constant SaO_2, which is consistent with data measurement and literature (27).] The mesh plot in Fig. 3*C* is the image on the $(P_{as}, \Delta O_2)$ plane of the Fig. 3*B* (H, W) mesh plot under this function $f(H,W)$ for generic, plausible values of physiological parameters (*SI Appendix*). Thus, any function $H = h(W)$ can be mapped from the (H, W) plane using model $(P_{as}, \Delta O_2) = f(H, W)$ to the $(P_{as}, \Delta O_2)$ plane to determine its consequences for the most important tradeoffs, which involve P_{as} and ΔO_2. These results are shown with the black lines in Fig. 3*B*, which give $H = h(W)$ curves consistent with Fig. 3*A* and then are mapped onto Fig. 3*C*.

Hidden complexity is unavoidable in the model $(P_{as}, \Delta O_2) = f(H, W)$, but we temporarily defer these details to focus on the general shape of the color-coded curves in Fig. 3 *B* and *C*, which have an intuitively clear explanation highlighted by the dashed red and purple lines. At constant workload, increased HR would greatly increase P_{as} while slightly decreasing ΔO_2 due to greater flow rate through the muscle. For constant HR, increased workload would greatly increase ΔO_2 while slightly reducing P_{as} due to greater oxygenation and peripheral vasodilatation. The cardiovascular control system adjusts HR as a function $H = h(W)$ of workload to tradeoff increasing P_{as} with increasing ΔO_2, both of which are undesirable. The modest curvature of the colored meshes in Fig. 3*C* demonstrates a small nonlinearity in the function $(P_{as}, \Delta O_2) = f(H, W)$. One source of this nonlinearity is the nonlinear relationship between cardiac output and HR due to less diastolic filling time as HR increases. However, the solid black lines in Fig. 3 manifest a much larger nonlinearity in the control function $H = h(W)$. We will argue that the essential sources of this nonlinearity are the tradeoff in robust homeostasis and metabolic efficiency and how it changes at different HR levels.

The hypothetical linear response at low workload in Fig. 3 can be explained in terms of purely metabolic tradeoffs. Healthy athletes can maintain the low workload almost indefinitely even in adverse (e.g., heat) conditions, a feature of human physiology thought to be an important adaptation for a successful hunter (39). Prolonged exercise necessarily requires steeply increased HR to provide sufficient tissue O_2 (low ΔO_2), to maintain aerobic lipid metabolism in muscles and preserve precious carbohydrates for the brain.

The nonlinear response in Fig. 3 (solid lines) reflects additional tradeoffs that arise at higher workload and HR, when the resulting high P_{as} becomes dangerous mainly due to actuator saturation of cerebral autoregulatory control. In healthy humans, CBF is autoregulated to be quite constant (28, 38) over a relatively wide range of P_{as} ($50 < P_{as} < 150$ mm Hg), so that no new tradeoffs at moderate exercise levels are required, because P_{as} is within this range. A new tradeoff does arise at P_{as} above 150 mm Hg when cerebral autoregulation saturates, and CBF begins to rise with the severe possible consequences of edema and/or hemorrhage. Thus, for the dashed black linear response in Fig. 3

Table 1. rms error for models of different complexity for data in Fig. 1

Row	No. parameters	Model structure	0–50 W	100–150 W	250–300 W
1	0	Zero: $h(W) = 0$	60.40	99.97	148.59
2	2	Global static: $h(W) = b{\cdot}W + C$	10.1	6.9	10.4
3	3 = 1 × 3	Piecewise constant $h_i(W) = C_i$	14.8	4.7	6.7
4	6 = 2 × 3	Piecewise static $h_i(W) = b_i{\cdot}W + C_i$	9.6	3.2	6.6
5	3	Global first order $\Delta h(t) = ah(t) + bW + C$	11.6	3.2	6.5
6	9 = 3 × 3	Piecewise first order $\Delta h_i(t) = ah_i(t) + b_iW + C_i$	8.9	2.1	0.9

Items in yellow highlight the best models balancing fitting error with model complexity. For the piecewise model, $i = 1,2,3$ stands for each exercise level, respectively; i.e., 0–50, 100–150, 250–300 W.

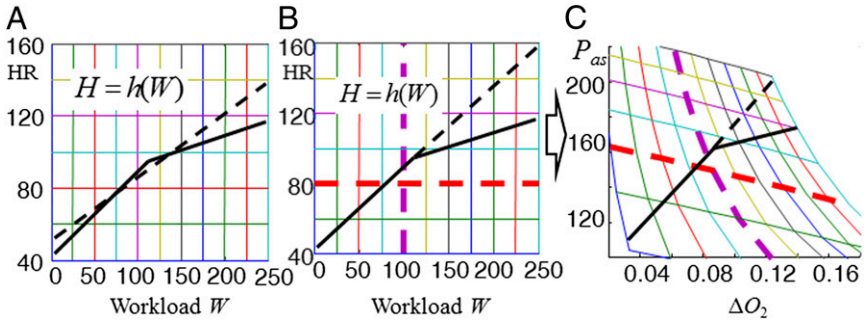

Fig. 3. Static analysis of cardiovascular control of aerobic metabolism as workload increases: Static data from Fig. 1*A* are summarized in *A* and the physiological model explaining the data is in *B* and *C*. The solid black curves in *A* and *B* are idealized (i.e., piecewise linear) and qualitatively typical values for $H = h(W)$ that are globally consistent with static piecewise linear fits (black in Fig. 1*A*) at the two lower workload levels. The dashed line in *A* shows $h(W)$ from the global static linear fit (blue in Fig. 1*A*) and in *B* shows a hypothetical but physiologically implausible linear continuation of increasing HR at the low workload level (solid line). The mesh plot in *C* depicts P_{as}–ΔO_2 (mean arterial blood pressure–tissue oxygen difference) on the plane of the *H*–*W* mesh plot in *B* using the physiological model $(P_{as}, \Delta O_2) = f(H, W)$ for generic, plausible values of physiological constants. Thus, any function $H = h(w)$ can be mapped from the *H*, *W* plane *(B)* using model *f* to the $(P, \Delta O_2)$ plane (*C*) to determine the consequences of P_{as} and ΔO_2. The reduction in slope of $H = h(W)$ with increasing workload is the simplest manifestation of changing HRV addressed in this study.

B and *C*, the resulting P_{as} would be elevated to potentially pathologic levels, and some nonlinearity as in the solid black line is necessary. Moreover, in many subjects there may be diminishing metabolic benefit of high tissue O_2 (low ΔO_2) at high workloads because muscle mitochondria saturate. Although many details of cerebral autoregulation (as well as the mitochondrial saturation) are poorly understood, the P_{as} at which autoregulation saturates is well-known in healthy adults, and helps to explain an important change in HRV with stressors. Ultimately, cardiac output itself saturates at sufficiently high HR due to compromised diastolic filling time with subsequent dramatic falls in stroke volume.

Mathematically, all these factors can be quantitatively reflected in a static optimization model using linear least squares, with $H = h(W)$ chosen to minimize a weighted penalty on increasing P_{as}, ΔO_2, and H:

$$\min\ q_P^2\left(P_{as}-P_{as}^*\right)^2+q_{o_2}^2\left(\Delta O_2-\Delta O_2^*\right)^2+q_H^2(H-H^*)^2$$

subject to linearization of the constraint $(P_{as}, \Delta O_2) = f(H, W)$ at 0 and 100 W. Here $P_{as}^*, \Delta O_2^*, H^*$ are the steady values for $P_{as}, \Delta O_2, H$ at 0 and 100 W, respectively. Different values for (q_P, q_{O_2}, q_H) reflect different tradeoffs between P_{as}, ΔO_2, and H at different workloads. In particular, q_P is higher at high workloads and high HR, reflecting the greater impact of P_{as} on CBF due to saturation of autoregulation, and q_H is higher to reflect the saturation of HR itself, which becomes more acute at higher workload levels. Straightforward, standard computations easily reproduce the piecewise linear features in Fig. 3 with higher penalty on P_{as} and H at higher workload levels.

An important feature of this approach is that it allows systematic exploration of models that are both simple and explanatory. We have systematically moved from the data in Fig. 1 to the fit in Fig. 3*A*, and then from very simple well-understood physiological mechanisms to how healthy HR should behave and be controlled, reflected in Fig. 3 *B* and *C*. The nonlinear behavior of HR is explained by combining explicit constraints in the form $(P_{as}, \Delta O_2) = f(H, W)$ due to well-understood physiology with constraints on homeostatic tradeoffs between rising P_{as} and ΔO_2 that change as W increases. The physiologic tradeoffs depicted in these models explain why a healthy neuroendocrine system would necessarily produce changes in HRV with stress, no matter how the remaining details are implemented. Taken together this could be called a "gray-box" model because it combines hard physiological constraints both in $(P_{as}, \Delta O_2) = f(H, W)$ and homeostatic tradeoffs to derive a resulting $H = h(W)$. If new tradeoffs not considered here are found to be significant, they can be added directly to the model as additional constraints, and solutions recomputed. The ability to include such physiological constraints and tradeoffs is far more essential to our approach than what is specifically modeled (e.g., that primarily metabolic tradeoffs at low HR shift priority to limiting P_{as} as cerebral autoregulation saturates at higher HR). This extensibility of the methodology will be emphasized throughout.

The most obvious limit in using static models is that they omit important transient dynamics in HR, missing what is arguably the most striking manifestations of changing HRV seen in Fig. 1. Fortunately, our method of combining data fitting, first-principles modeling, and constrained optimization readily extends beyond static models. The tradeoffs in robust efficiency in P_{as} and ΔO_2 that explain changes in HRV at different workloads also extend directly to the dynamic case as demonstrated later.

Dynamic Fits. In this section we extract more dynamic information from the exercise data. The fluctuating perturbations in workload (Fig. 1) imposed on a constant background (stress) are targeted to expose essential dynamics, first captured with "black-box" input–output dynamic versions of above static fits. Fig. 1*B* shows the simulated output $H(t)$ = HR (in black) of simple local (piecewise) linear dynamics (with discrete time t in seconds)

$$\Delta H(t) = H(t+1) - H(t) = Hh(t) + bW(t) + c, \qquad [1]$$

where the input is $W(t)$ = workload (blue). Constants (a, b, c) are fit to minimize the rms error between $H(t)$ and HR data as before (Table 1). The optimal parameter values $(a, b, c) \sim (-0.22, 0.11, 10)$ at 0 W differ greatly from those at 100 W $(-0.06, 0.012, 4.6)$ and at 250 W $(-0.003, 0.003, -0.27)$, so a single model equally fitting all workload levels is necessarily nonlinear. This conclusion is confirmed by simulating HR (blue in Fig. 1*B*) with one best global linear fit $(a, b, c) \sim (0.06, 0.02, 2.93)$ to all three exercises, which has large errors at high and low workload levels.

The changes of the large, slow fluctuations in both HR (red) and its simulation (black) in Fig. 1*B* are consistent with well-understood cardiovascular physiology, and illustrate how the physiologic system has evolved to maintain homeostasis despite stresses from workloads. Our next step in modeling is to mechanistically explain as much of the HRV changes in Fig. 1 as possible using only standard models of aerobic cardiovascular physiology and control (27–31). This step focuses on the changes in HRV in the fits in Fig. 1*B* (in black) and Eq. **1**, and we defer

modeling of the high-frequency variability in Fig. 1 until later (i.e., the differences between the red data and black simulations in Fig. 1*B*).

The black-box fits allow us to plausibly conjecture that workload disturbances cause most of the variability in Fig. 1*B* (black curves). Here the rigor of the black-box fits is important, as highlighted by three features: (*i*) no comparably good fits exist for the data in Fig. 1 without the input of workload, (*ii*) within the limits of the sensors used and subject fitness we can otherwise experimentally manipulate the input independently and over a wide range to make it truly a "causal" input, and (*iii*) the fits accurately predict the HR output response to new experiments (i.e., cross-validation; see *SI Appendix*).

First-Principles Models. Our first-principles model is based on the circulatory circuit diagram in Fig. 2, using standard mathematical descriptions of circulation, and with a focus on modeling purely aerobic exercise. That is, we only model blood flow, blood pressure, and O_2 in several compartments, and yet the model captures the overall physiologic HR response during moderate exercise in young, fit adults. In standard models of aerobic cardiovascular control (27–31) the neuroendocrine system controls peripheral vasodilation, minute ventilation, and cardiac output to maintain blood pressure and oxygen saturation within acceptable physiological limits.

Several features of these control systems allow substantial simplification of the model. Minute ventilation $\dot{V}_E$ alone can tightly control arterial oxygenation $[O_2]_a$, so we assume $[O_2]_a$ is maintained nearly constant (27). Moreover, peripheral resistance R_s is decreased during exercise and the decrease is determined by local metabolic control. The purpose of decreasing R_s in the arterioles is to increase blood flow and regional delivery of O_2, glucose, and other substrates as needed. Because the venous oxygenation $[O_2]_v$ serves as a good signal for oxygen consumption, we also assume that control of peripheral vascular resistance R_s is a function only of venous oxygenation $[O_2]_v$ (31).

Combined with those models for blood circulation and oxygen consumption, we have the following physiological model:

$$\begin{aligned} V_{as} &= c_{as}\cdot P_{as} & Q_l &= c_l\cdot H\cdot P_{vp}\\ V_{vs} &= c_{vs}\cdot P_{vs} & Q_r &= c_r\cdot H\cdot P_{vs}\\ V_{ap} &= c_{ap}\cdot P_{ap} & F_s &= (P_{as}-P_{vs})/R_s\\ V_{vp} &= c_{vp}\cdot P_{vp} & F_p &= (P_{ap}-P_{vp})/R_p\\ V_{tot} &= V_{as}+V_{vs}+V_{ap}+V_{vp} & M &= \rho\cdot W+M_0\\ [O_2]_a &= 0.2 & R_s &= A\cdot[O_2]_v+R_{s0}. \end{aligned} \quad [2]$$

Here V and P are (subscripts a = arterial, v = venous, s = systemic, P = pulmonary) blood volume and blood pressure, respectively. All of the c variables are constants. The main elements of the model are (more details in *SI Appendix*): (*i*) arterial and venous compartments of systemic and pulmonary circulations are treated as compliant vessels, modeled in the form $V = c{\cdot}P$, with the total blood volume a constant V_{tot}; (*ii*) cardiac output of the left (Q_l) and right (Q_r) ventricles; (*iii*) blood flow for systemic (F_s) and pulmonary (F_p) circulation; (*iv*) the metabolic consumption M; (*v*) $[O_2]_a$ and R_s are modeled according to the previous description of the control mechanism. Note that we need not model these control systems in detail, but simply extract their most well-known features and use them to constrain the model.

In steady state the follow additional constraints hold:

$$\begin{aligned} Q_r &= Q_l = F_s = F_p\\ M &= F_s\left([O_2]_a-[O_2]_v\right) \end{aligned} \quad [3]$$

The first equation is total blood circulation balance and the second one is based on the oxygen circulation balance, where $F_s([O_2]_a - [O_2]_v)$ is the net change in the arterial and venous blood O_2 content. The oxygen drop ΔO_2 across the muscle bed is defined as $\Delta O_2 = [O_2]_a - [O_2]_v$. Combining **2** and **3** plus simple algebra (*SI Appendix*) gives the steady-state model $(P_{as}, \Delta O_2) = f(H, W)$ shown in Fig. 3 that constrains the relationship between $(P_{as}, \Delta O_2)$ and (H, W).

In general the circulatory system is far from steady state in our experiments. Modeling the blood volume change for each circulatory compartment and the oxygen change in the tissue keeps the constraints from Eq. **2** but replaces **3** with the following dynamic model:

$$\begin{aligned} c_{as}\dot{P}_{as} &= Q_l - F_s\\ c_{vs}\dot{P}_{vs} &= F_s - Q_r\\ c_{ap}\dot{P}_{ap} &= Q_r - F_p\\ v_{T,O_2}\left[\dot{O}_2\right]_v &= -M + F_s\cdot\left([O_2]_a-[O_2]_v\right)\\ c_{vp}P_{vp} &= V_{total}-\left(c_{as}P_{as}+c_{vs}P_{vs}+c_{ap}P_{ap}\right). \end{aligned} \quad [4]$$

Here v_{T,O_2} denotes the effective tissue O_2 volume and we assume that tissues and venous blood gases are in equilibrium, namely that tissue oxygenation $[O_2]_T$ is the same as venous oxygenation $[O_2]_v$ (*SI Appendix*). The previous static analysis (and the purely static tradeoffs it highlights) directly extends to the dynamic case with modestly increased complexity. The simplest extension is to use an optimal linear quadratic state feedback controller (34) for linearizations of **4** at 0 and 100 W, with controller $H = u(\cdot)$ chosen to minimize a weighted penalty on integrated elevation of P_{as}, ΔO_2, and H:

$$\min\int\left(q_P^2\left(P_{as}-P_{as}^*\right)^2+q_{o_2}^2\left(\Delta O_2-\Delta O_2^*\right)^2+q_H^2\left(H-H^*\right)^2\right)dt \quad [5]$$

subject to linearizations of the state dynamic constraint **4**. Fig. 4 compares HR and workload data versus simulations of applying the linear controllers to the model in **4** for two experiments

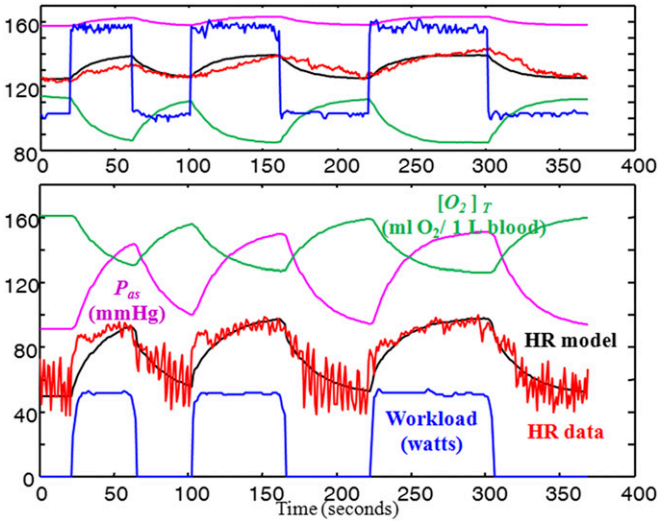

Fig. 4. Optimal control model response using first-principle model to two different workload (blue) demands, approximately square waves of 0–50 W (*Lower*) and 100–150 W (*Upper*): For each data set (using subject 2's data), a physiological model with optimal controller is simulated with workload as input (blue) and HR (black) as output, and compared with collected HR data (red). Simulations of blood pressure (P_{as}, purple) and tissue oxygen saturation ($[O_2]_T$, green) are consistent with the literature but data were not collected from subjects. Breathing is spontaneous (not controlled).

(similar to Fig. 1 but with a different subject) with higher penalty on P_{as} and H at higher workloads as in the static case. (See *SI Appendix* for more details.) Also shown are simulations of P_{as} and $[O_2]_T$, which are consistent with the literature but were not measured. The same methods and results apply to other subjects' data and new experiments (e.g., cross-validation; see *SI Appendix*.). Also note that for different subjects, we use the same nominal values for most parameters except the constants c_r,c_l used in the cardio-output formulation and the weighting parameters q_P, q_{O_2}, q_H used in the tradeoff function **5**. The different c_r,c_l reflect the different sizes of subjects and different q_P, q_{O_2}, q_H reflect the qualitative differences in the control objectives.

The change in the tradeoff as workload increases is consistent with what we observed using the static model. At low workload and low HR, the main tradeoff is metabolic because both P_{as} and HR are at safe and sustainable levels. High HR and thus high $[O_2]_T$, (low ΔO_2), maintains aerobic muscle metabolism, extending the potential duration of exercise while preserving carbohydrate resources for the brain. At higher workloads, this strategy would produce unsustainably high and potentially damaging P_{as} and possibly HR, so the optimal controller penalizes these factors more, at the price of reduced $[O_2]_T$. HRV (slow time scale) in Fig. 1 (and P_{as} in Fig. 4) decreases with increasing workload because of the changing tradeoffs between metabolic overhead and P_{as}, ΔO_2, and H as their means increase. These explanations in HRV derived from the dynamic aerobic model are richer and more complete but due to the same tradeoffs as in the simpler static model.

Importantly, although the mathematics and physiology required are relatively elementary and the resulting explanation is intuitively clear and mechanistic, they nonetheless highlight the rigor and scalability of this approach. The simplicity of the black-box fits in **1** and Fig. 1 helps establish causal relationships between variables and suggests physiological mechanisms to model in more detail, and highlights features in the signals that are not modeled (i.e., we have not explained the high frequency of the signals at low watts in Fig. 1, considered in the next sections). The hard homeostatic tradeoffs and the actuator effects of HR, ventilation, and vasodilation were included in the physiology model in **2**–**5** but the neuroendocrine implementation details were not. Also, the impact of cerebral autoregulatory saturation was included, but the details of implementation were not. Nonetheless, this approach allows for clinically actionable explanations that do not depend on poorly understood mechanisms peripheral to the component being modeled, and provides a framework for systematically refining such models using a similar (but presumably vastly more complex) combination of black- and gray-box models and physiology. Again, if new tradeoffs not considered here are found to be significant, they can be added directly as additional constraints are recognized and solutions recomputed. Further, tradeoffs may well change as organ systems fail, when these models are extended to disease states.

High-Frequency HRV. The high-frequency fluctuations in HR that are particularly large at low mean workloads and low HR cannot be explained by the simple fits or models above, and thus additional signals and mechanisms must be included that can be causally related to this setting. Figs. 5 and 6 shed light on breathing as a cause of much of the high-frequency HRV. Fig. 5*A* shows HR (red) during natural breathing at rest, with the

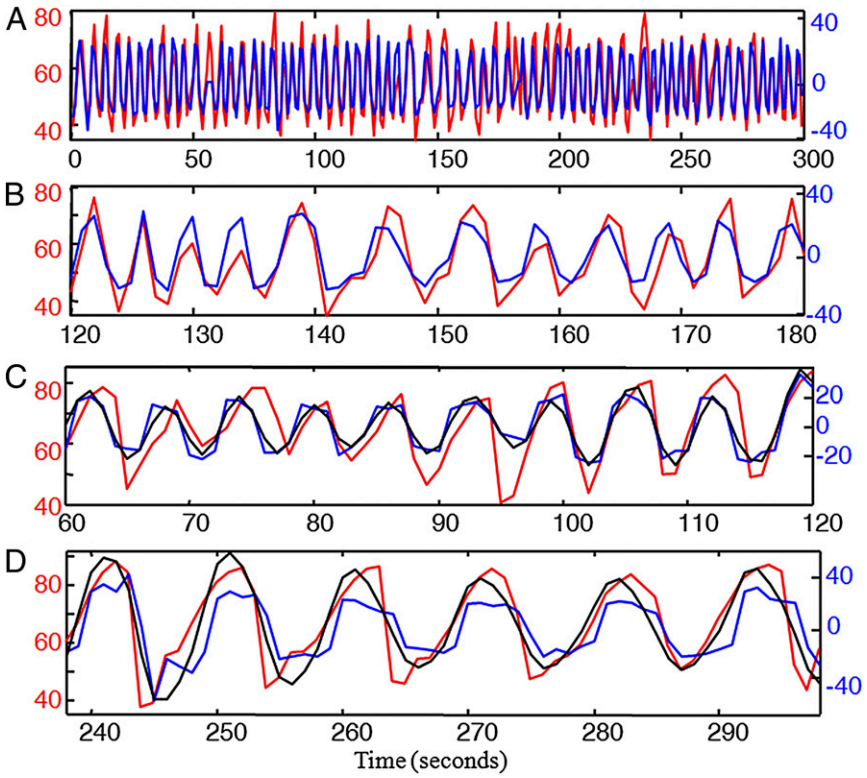

Fig. 5. HR response (red) to ventilation V (blue) at rest (0 W): The ventilatory data are raw speed of inhalation and exhalation measured at the mouthpiece. In each case the units for V (blue) are chosen to show the optimal static fit $h(V) = b{\cdot}V + c$ to the collected HR data. *A* and *B* show natural breathing, with *B* zoomed in to focus on a smaller window to help visualize the data and fit. *C* and *D* are similar focused smaller windows from a longer controlled breathing experiment at resting (0 W) where the subject followed a frequency sweep from fast to slow breathing (see Fig. 6 for the full frequency range). *C* focuses on breathing frequencies close to natural breathing, whereas *D* focuses on frequencies slower than natural. Both *C* and *D* show simulated dynamic fits (black), and optimal static fits $h(V) = b{\cdot}V + C$ (blue). The dynamic fits improve on the static fits more for the controlled sweep than for natural breathing (Table 2).

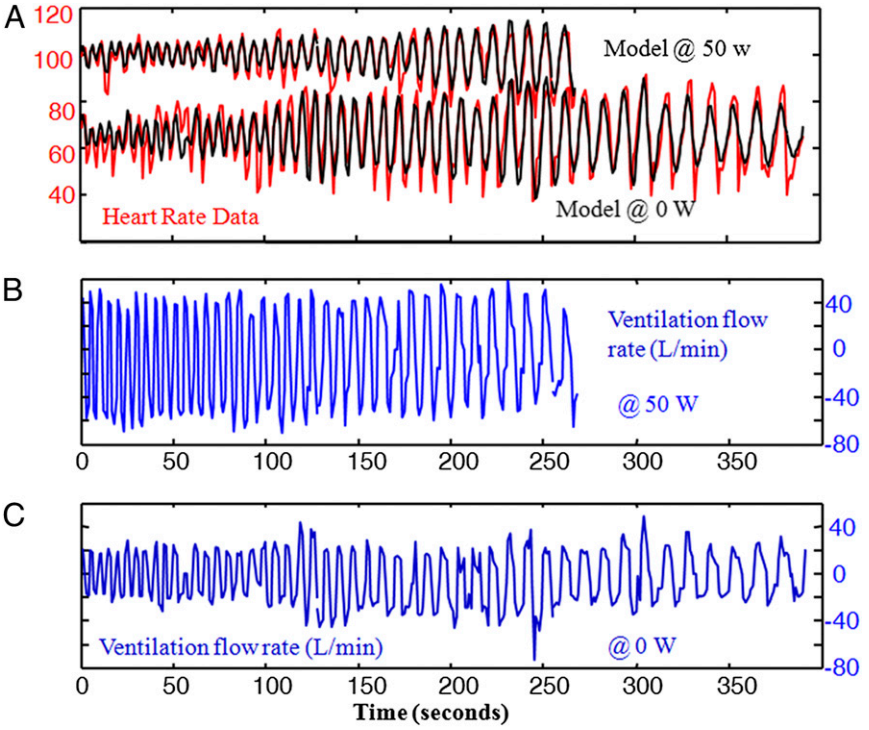

Fig. 6. HR response to sweep ventilation on different workload levels: Two experiments with *(A)* HR (red) and dynamic fit (black) to input of controlled ventilation frequency sweeps with measured ventilatory flow rate (blue) on a fixed background workload of (*B*) 0 W or (*C*) 50 W. Ventilatory flow (with spontaneous ventilation magnitude) was necessarily larger at 50 W and the subject was unable to breathe slowly enough to complete the entire frequency sweep.

optimal static fit $H = h(V) = b{\cdot}V + c$, where V (blue) is measured ventilation flow rates (inhalation and exhalation) at the mouthpiece. The static linear fit can be used to scale the units of V (blue) in Fig. 5*A* to visualize the best fit to HR (red) and its error, shown in Table 2. That HR and ventilation match so well in frequency is consistent with the observation that under certain conditions, inspiration is accompanied by an acceleration of HR, and expiration by a deceleration, a phenomenon called respiratory sinus arrhythmia (RSA) (16, 40–46). However, because ventilation and HR are both generated by neuroendocrine control, this fit (i.e., correlation) by itself does not suggest a specific mechanistic explanation of the resulting ventilation–HR correlation or HRV.

To sharpen this picture, Fig. 6 shows data from subjects instructed to control respiratory rate (RR, shown in blue) by following a computer-generated RR frequency sweep (tidal volumes not controlled), repeated with a background of 0- and 50-W exercises, respectively. (Fig. 5*B* shows HR and zoomed in for the 0-W exercise data.) For each exercise taken separately, HR is fit with static (blue in Fig. 5*B*) and one-state models, as well as a two-state, five-parameter linear model (shown in black in Figs. 5*B* and 6, Table 2):

$$\begin{aligned}\Delta H(t) &= a_1 H(t) + b_1 V(t) + x(t)\\ \Delta x(t) &= a_2 x(t) + b_2 V(t) + c\end{aligned},$$

where V is ventilatory flow rates, x is an internal black-box state, and the parameters depend on workload. Whereas breathing cannot be varied as systematically and widely as workload, these black-box fits provide strong evidence that ventilation is the main factor causing high-frequency HRV. The underlying physiological mechanisms remain unclear, but we now know where to look next. In Fig. 6, minute ventilation naturally increases at 50 W, yet HRV goes down, a nonlinear pattern consistent with the trends in Figs. 1 and 3, but more dramatic. As Table 2 shows, dynamic fits have little benefit for natural breathing at rest, but modestly reduce the error for the controlled respiratory sweeps at low- and high-frequency breathing. In all cases, the frequency of HR oscillations is fit better than the magnitude, suggesting both a dynamic and nonlinear dependence of HR on ventilatory flow rates.

Although RSA magnitude has been used as a measure of vagal function, after many years of research the mechanism of RSA, e.g., whether RSA is due to a central or a baroreflex mechanism, is still debated (16, 40–46). Moreover, the data and dynamic fits show a small resonant peak in the frequency response at around 0.1 Hz at 0 W, and the significance of the peak is unclear. Of note, this characteristic peak occurred in the fits for every subject (although the exact RR at which it occurs varied), and is consistent with observations in the literature (16, 40). (In *SI Appendix*, we also use both workload and ventilation data as inputs to fit HR data during the easy workout in Fig. 1.)

Resolution of these mysteries requires additional measurements such as arterial blood pressure (more invasive human studies), more sophisticated physiological modeling including the mechanical effects of breathing on arterial blood pressure and pulmonary stretch reflexes, plus changing tradeoffs in control of arterial blood pressure at different workloads and HR levels. In particular, model **2**–**5** above assumed continuous ventilation and HRs (i.e., no intrabreath or -beat dynamics), so more detailed modeling of physiological respiratory patterns and their mechanical and metabolic effects is needed.

Discussion

Robust Efficiency and Actuator Saturation. We showed how HR fluctuations in healthy athletes can be largely explained as nonlinear dynamic, but not chaotic, responses to either external (e.g., workload) or internal (e.g., ventilation implemented by pulsatile breathing) disturbance. We provided mechanistic explanations and plausible conjectures for essentially all of the HRV in Fig. 1, and showed that changes in HRV per se, no matter how mea-

Table 2. rms error for models of different complexity for data in Figs. 5 and 6

Row no.	No. prms	Model structure	Resting natural	Resting sweep	50-W sweep
1	0	Zero	56	67	98
2	1	Constant	11.6	13.1	7.9
3	2	Static	6.4	9.7	5.9
4	3	First-order dynamic	6.0	9.7	5.5
5	6	Second-order dynamic	6.0	7.5	4.0

Items in yellow highlight the best models balancing fitting error with model complexity.

sured, are much less important mechanistically than the tradeoffs that produce them. The tradeoffs we highlight between robustness, homeostasis, and metabolic efficiency are universal and essential (1, 23) features of complex systems but can remain hidden and cryptic (47) without an appropriate mathematical framework (4, 48). "Universal" features illustrated by this physiological (HR) control system include how efficiently maintaining robust homeostasis (e.g., small errors in CBF, S_aO_2, and ΔO_2) in the presence of large disturbances requires correspondingly large actuator (e.g., HR, ventilation, and cerebral autoregulation) responses to compensate, and how nonlinearities in actuator saturations lead to reductions in actuator activity (e.g., HRV) under increased load or stress.

HR control and HRV highlight layered control, actuator constraints, and hard tradeoffs of the type that pervade physiology and are generally fundamental in complex control systems. In summary, actuators are the mechanisms by which controllers act on the system to provide efficient performance and robust homeostasis. In the cardiovascular models so far, the most important saturation is in cerebral autoregulation, which forces a nonlinear change in $H = h(W)$ as workload increases to avoid high P_{as} that leads to intracerebral pathology (edema, hemorrhagic stroke).

Further understanding of control complexity and the role of actuator (e.g., HR) variability and saturation in physiologic control comes from examination of other technological examples of complex systems. Familiar examples include automobiles, particularly new autonomous robotic versions. A car is moved and controlled via the actuators that produce and deliver power, braking, and steering that result in accelerations in forward, backward, and lateral directions. Most complexity in an autonomous robot car is in the control system for robust efficiency to uncertainty in real traffic environments and to intrinsic variability in components. If scientists were forced to "reverse engineer" such a car without access to the forward engineering process, they would likely study "knockouts" of components to infer their function, and also push the vehicles to extremes to find the limits of their robust performance. It would be surprising if "reverse engineering" cardiovascular control would be easier than a robot car, or could be accomplished with less sophisticated tools and without domain-specific details.

Loss of car actuator variability due to "stress" parallels loss of HRV, in that it is loss of actuator responsiveness that causes deterioration of function, and loss of variability is only a symptom of actuator dysfunction. Currently, human drivers cause most crashes when they reduce their actuator responsiveness because of multitasking, alcohol consumption, fatigue, or poor visibility, or when surface conditions make the actuators less effective. Automatic collision avoidance and antilock and antislip traction control systems mitigate these effects, and augment human control in emergencies. However, even in fully automated robotic cars with robust control systems, at extremes of speed, acceleration, braking, and turning (such as a race scenario or in icy conditions), actuators would frequently saturate and lose variability, resulting in less maneuverability, and an increase in errors and risk of crashes. Thus, actuator saturation causing changes in variability is a "signature" of a wide variety of dangerous scenarios, and essential to understanding vehicle limits and malfunction. However, variability per se is unimportant, and analyzing the statistics of individual signals (e.g., fuel or air rates, braking, acceleration, turning rate, etc.) in isolation is relatively less diagnostic compared with understanding integrated, mechanistic dynamic models of signal interactions.

Similar tradeoffs to those resulting in HRV are found throughout technology and biology. For example, glycolytic oscillations were one of the most persistent mysteries involving dynamics in cell biology (1). The proximal role of how autocatalytic and regulatory feedbacks make oscillations possible was well understood, but the unresolved deeper "why" question was the purpose of the oscillations, or alternatively, whether they were just frozen accidents of evolution. Oscillations are neither functional nor accidental but are a side effect of provably hard tradeoffs involving efficiency and robust control (1). The glycolysis circuit must maintain adequate ATP concentrations that are robust to fluctuations in demand and to enzyme and other metabolite levels. It must also be metabolically efficient, in the sense of not requiring excessive enzyme concentrations. Any circuit that aims to balance these competing requirements has the potential to oscillate, particularly when enzymes saturate.

Mathematical Framework. It has been difficult to characterize multilayered aspects of biological control, but our approach is aimed at providing tools for biologists and clinicians, combining established principles of system identification fits and control theory with basic physiological models. The fits in Figs. 1, 5, and 6 highlight causal input–output relationships between variables and help suggest the relevant physiology. By comparison, even the most sophisticated statistical analysis of individual HR signals taken out of physiologic context is mechanistically uninformative. In contrast, the static and dynamic models mechanistically explain Figs. 3 and 4 and most of the variability in Fig. 1 (i.e., the black curves at the lower two watts). Our explanation in terms of aerobic metabolism is simple and intuitive as well as mechanistic, and requires only basic mathematics and physiology. The main requirement of the models is some mechanistic relationship between control actuation and its limits in maintaining robust homeostasis. Thus, we did not need detailed understanding of neuroendocrine control implementation or peripheral autoregulation, but only that they adequately manage the tradeoffs and saturation effects in muscle, brain, and heart as described above. Moreover, specific details of the computational approach, e.g., piecewise linear least squares used in this paper, are not essential to understanding the underlying system control. What is important is that the right constraints are properly reflected in the computation, so that the resulting controller function is constrained by the right physiological mechanisms plus appropriately changing penalties–constraints on vital physiological variables due to metabolic tradeoffs and limit.

Our approach also importantly highlights where mechanisms are missing. The model in **2**–**5** and Fig. 4 assume continuous ventilation and HRs (i.e., no intrabreath or -beat dynamics) and do not capture any of the higher frequency HRV in Fig. 1. The fits in Figs. 5 and 6 suggest that the dynamics of physiological respiratory patterns and their mechanical and metabolic effects

are necessary and perhaps sufficient to explain the high-frequency HRV seen in Fig. 1. There may also be connections between robust efficiency and oscillations as in ref. 1 to explain the origin of the peaks in frequency response of the breath-to-HR fits.

An essential feature of this project is that our tools be robust and scalable to more complex signals and models, and that if new mechanisms and/or tradeoffs are discovered that are important, they can be added as additional constraints. Fortunately, we can leverage enormous recent advances in engineering theory and practice, although these remain largely unknown in mainstream science outside of the most advanced parts of systems biology. The general models and methods, particularly moving from **1** to **2–5** (and Fig. 1 to Figs. 3 and 4), used for this relatively straightforward study should serve well as a foundational framework for the evaluation of even more complex physiologic (disease) situations in which the diagnostic possibilities are broader.

Clinical Correlates: Linking the Behavior of Control Systems and Pathophysiology. Clinicians know that changes in actuator signals (e.g., HR increases) can signify a great variety of potentially important derangements such as hypovolemia, congestive heart failure, inflammation, sepsis, etc. (6–13). Even without specific diagnostic content, alerts to clinicians that HRV is changing can be useful. Such an alert has been incorporated into monitoring of premature neonates. In this case, monitoring of HR characteristics is used to report a statistic that reflects the performance of the actuator mechanisms. The utilization of this statistic by clinicians was sufficient to change practice (i.e., reevaluation of the patient with consideration of need for additional therapies) and achieve a significant improvement in outcomes (10, 13). This particular example of integration of mathematical analysis into monitors represents a special situation because the alert also incorporates the occurrence of cardiac decelerations, a phenomenon not observed in adults. Furthermore, because sepsis is a common problem in this setting, the clinicians chose to administer antimicrobial therapy on the basis of the alert which produced the outcome benefit. In fact, the efficacy of the monitor in early sepsis detection was subsequently demonstrated in a post hoc analysis (13). However, in most clinical scenarios, actuator changes alone are usually so generic that they lack specific diagnostic value, and extensive analyses of individual time series have not yielded mechanistic explanations that can narrow the diagnosis (6–12).

In contrast, the general type of models and methods used here and the application of control theory to physiology present an enormous opportunity to reexamine this area with powerful mathematical tools and a systems engineering approach (48). This is important because system dysfunction is manifested earlier in the behavior of the control system than in any metric associated with the system's output. The long-term goal of this research is earlier diagnosis afforded by monitoring control elements in addition to individual signal outputs.

Materials and Methods

After Caltech Institutional Review Board approval, five fit athletic subjects (ages 25–35 y, three men and two women) performed a series of experimental exercise regimens, each on two different days. The intensity and durations were less than routine training for these athletes, and they had used the laboratory equipment before so were familiar and comfortable with the environment. In all experiments, the subject pedaled a Life Fitness stationary recumbent bicycle at near-constant speed with the pedaling resistance controlled by a preprogrammed protocol. In the respiration rate (RR) sweep experiments, a sinusoid signal was preprogrammed in the computer with frequency from 2 Hz to 0.06 Hz and each subject watched the signal and controlled RR to follow the frequency of the signal until they were unable to continue.

In all exercise tests, 1-Hz work rate data were recorded from a Life Fitness stationary recumbent exercise bicycle interfaced with a computer running MATLAB via the Communications Specification for Fitness Equipment protocol. Other exercise testing data were collected using commercially available noninvasive monitors. (*i*) RR interval HR data were recorded with a Polar heart rate monitor and converted to 1-Hz HR data using the integral pulse frequency modulation model (49). (*ii*) In the tests shown in Figs. 5 and 6, 100-Hz ventilation (inhalation and exhalation) flow rate data were recorded with a Philips $NiCO_2$ monitor, and down-sampled to 1-Hz ventilation flow rate data. (*iii*) In the test shown in Fig. 7, 1-Hz gas data including minute ventilation $\dot{V}_E$, oxygen consumption $\dot{V}O_2$ and carbon dioxide generation $\dot{V}CO_2$ were collected with a Vacumetrics monitor and TurboFit software. No other preprocessing of data was performed.

A detailed discussion of mathematical methods is given in *SI Appendix*.

ACKNOWLEDGMENTS. We thank Pamela B. Pesenti for her gift in establishing the John G. Braun Professorship, which supported this research, and Philips for providing equipment used in the experiments. The research progress has been presented and discussed at several meetings, including the International Conference on Complexity in Acute Illness of the Society for Complexity in Acute Illness (SCAI). Comments from many SCAI members greatly influenced this paper. We also thank the athletes who were the subjects for this study. The theoretical aspects of this work and the connections with other complex systems challenges were supported in part by Air Force Office of Scientific Research and National Science Foundation. Preliminary exploration in this research direction was funded by Pfizer, National Institutes of Health (R01 GM078992), and the Institute of Collaborative Biotechnologies (ARO W911NF-09-D-0001).

1. Chandra FA, Buzi G, Doyle JC (2011) Glycolytic oscillations and limits on robust efficiency. *Science* 333(6039):187–192.
2. Pool R (1989) Is it healthy to be chaotic? *Science* 243(4891):604–607.
3. Buzsáki G (2006) *Rhythms of the Brain* (Oxford Univ Press, New York).
4. Glass L (2001) Synchronization and rhythmic processes in physiology. *Nature* 410(6825): 277–284.
5. Buchman TG (2002) The community of the self. *Nature* 420(6912):246–251.
6. Goldberger AL, et al. (2002) Fractal dynamics in physiology: alterations with disease and aging. *Proc Natl Acad Sci USA* 99(Suppl 1):2466–2472.
7. Camm AJ, et al.; Task Force of the European Society of Cardiology and the North American Society of Pacing and Electrophysiology (1996) Heart rate variability: Standards of measurement, physiological interpretation and clinical use. *Circulation* 93(5):1043–1065.
8. Ivanov PC, et al. (1999) Multifractality in human heartbeat dynamics. *Nature* 399(6735):461–465.
9. Poon CS, Merrill CK (1997) Decrease of cardiac chaos in congestive heart failure. *Nature* 389(6650):492–495.
10. Moorman JR, et al. (2011) Cardiovascular oscillations at the bedside: Early diagnosis of neonatal sepsis using heart rate characteristics monitoring. *Physiol Meas* 32(11):1821–1832.
11. Tulppo MP, Mäkikallio TH, Takala TE, Seppänen T, Huikuri HV (1996) Quantitative beat-to-beat analysis of heart rate dynamics during exercise. *Am J Physiol* 271(1 Pt 2): H244–H252.
12. Yamamoto Y, Hughson RL, Peterson JC (1991) Autonomic control of heart rate during exercise studied by heart rate variability spectral analysis. *J Appl Physiol (1985)* 71(3): 1136–1142.
13. Moorman JR, et al. (2011) Mortality reduction by heart rate characteristic monitoring in very low birth weight neonates: A randomized trial. *J Pediatr* 159(6):900–906.e1.
14. Akselrod S, et al. (1981) Power spectrum analysis of heart rate fluctuation: A quantitative probe of beat-to-beat cardiovascular control. *Science* 213(4504):220–222.
15. Mackey MC, Glass L (1977) Oscillation and chaos in physiological control systems. *Science* 197(4300):287–289.
16. Novak V, et al. (1993) Influence of respiration on heart rate and blood pressure fluctuations. *J Appl Physiol* 74(2):617–626.
17. Gierałtowski J, Żebrowski JJ, Baranowski R (2012) Multiscale multifractal analysis of heart rate variability recordings with a large number of occurrences of arrhythmia. *Phys Rev E Stat Nonlin Soft Matter Phys* 85(2 Pt 1):021915.
18. Barabási AL (2009) Scale-free networks: A decade and beyond. *Science* 325(5939): 412–413.
19. Glass L (2009) Introduction to controversial topics in nonlinear science: Is the normal heart rate chaotic? *Chaos* 19(2):028501.
20. Kluttig A, Kuss O, Greiser KH (2010) Ignoring lack of association of heart rate variability with cardiovascular disease and risk factors: Response to the manuscript "The relationship of autonomic imbalance, heart rate variability cardiovascular disease risk factors" by Julian F. Thayer, Shelby S. Yamamoto, Jos F. Brosschot. *Int J Cardiol* 145(2):375–376.
21. Young NS, Ioannidis JPA, Al-Ubaydli O (2008) Why current publication practices may distort science. *PLoS Med* 5(10):e201.
22. Stumpf MPH, Porter MA (2012) Mathematics. Critical truths about power laws. *Science* 335(6069):665–666.
23. Alderson DL, Doyle JC (2010) Contrasting views of complexity and their implications for network-centric infrastructures. *IEEE Transactions on Systems, Man and Cybernetics, Part A: Systems and Humans* 40(4):839–852.
24. Ioannidis JPA (2005) Why most published research findings are false. *PLoS Med* 2(8):e124.

25. Wigertz O (1970) Dynamics of ventilation and heart rate in response to sinusoidal work load in man. *J Appl Physiol* 29(2):208–218.
26. Warner HR, Cox A (1962) A mathematical model of heart rate control by sympathetic and vagus efferent information. *J Appl Physiol* 17(2):349–355.
27. Brooks GA, Fahey TD, Baldwin K (2004) *Exercise Physiology: Human Bioenergetics and Its Applications* (McGraw–Hill, New York).
28. Rowell LB (1993) *Human Cardiovascular Control* (Oxford Univ Press, New York).
29. Grodins FS, Buell J, Bart AJ (1967) Mathematical analysis and digital simulation of the respiratory control system. *J Appl Physiol* 22(2):260–276.
30. Guyton A, Hall J (2006) *Textbook of Medical Physiology* (Elsevier Saunders, Philadelphia), 11th Ed.
31. Hoppensteadt FC, Peskin CS (2002) *Modeling and Simulation in Medicine and the Life Sciences* (Springer, New York).
32. Batzel JJ, Schneditz D (2007) *Cardiovascular and Respiratory Systems: Modeling, Analysis, and Control* (Society for Industrial and Applied Mathematics, Philadelphia).
33. Ljung L (1999) *System Identification: Theory for the User* (Prentice Hall, Upper Saddle River, NJ).
34. Kirk D (2004) *Optimal Control Theory: An Introduction* (Dover, New York).
35. Doya K, Ishii S, Pouget A, Rao RPN, eds. (2007) *Bayesian Brain: Probabilistic Approaches to Neural Coding*. (MIT Press, Cambridge, MA).
36. Cheng TM, Savkin AV, Celler BG, Su SW, Wang L (2008) Nonlinear modeling and control of human heart rate response during exercise with various work load intensities. *IEEE Trans Biomed Eng* 55(11):2499–2508.
37. Mullen TJ, Appel ML, Mukkamala R, Mathias JM, Cohen RJ (1997) System identification of closed-loop cardiovascular control: Effects of posture and autonomic blockade. *Am J Physiol* 272(1 Pt 2):H448–H461.
38. Paulson OB, Strandgaard S, Edvinsson L (1990) Cerebral autoregulation. *Cerebrovasc Brain Metab Rev* 2(2):161–192.
39. Bramble DM, Lieberman DE (2004) Endurance running and the evolution of Homo. *Nature* 432(7015):345–352.
40. Mehlsen J, Pagh K, Nielsen JS, Sestoft L, Nielsen SL (1987) Heart rate response to breathing: Dependency upon breathing pattern. *Clin Physiol* 7(2):115–124.
41. Hirsch JA, Bishop B (1981) Respiratory sinus arrhythmia in humans: How breathing pattern modulates heart rate. *Am J Physiol* 241(4):H620–H629.
42. Eckberg DL (1983) Human sinus arrhythmia as an index of vagal cardiac outflow. *J Appl Physiol* 54(4):961–966.
43. Schäfer C, Rosenblum MG, Kurths J, Abel HH (1998) Heartbeat synchronized with ventilation. *Nature* 392(6673):239–240.
44. Grossman P, Karemaker J, Wieling W (1991) Prediction of tonic parasympathetic cardiac control using respiratory sinus arrhythmia: The need for respiratory control. *Psychophysiology* 28(2):201–216.
45. Berntson GG, Cacioppo JT, Quigley KS (1993) Respiratory sinus arrhythmia: Autonomic origins, physiological mechanisms, and psychophysiological implications. *Psychophysiology* 30(2):183–196.
46. Eckberg DL (2009) Point:counterpoint: Respiratory sinus arrhythmia is due to a central mechanism vs. respiratory sinus arrhythmia is due to the baroreflex mechanism. *J Appl Physiol (1985)* 106(5):1740–1742, discussion 1744.
47. Doyle JC, Csete M (2011) Architecture, constraints, and behavior. *Proc Natl Acad Sci USA* 108(Suppl 3):15624–15630.
48. Winslow RL, Trayanova N, Geman D, Miller MI (2012) Computational medicine: Translating models to clinical care. *Sci Trans Med* 4(158):158rv111.
49. Han K, Nagel JH, Schneiderman N (1992) A continuous representation of heart rate. *Engineering in Medicine and Biology Society, 1992. 14th Annual International Conference of the IEEE* 2:785–786.

Supporting Information Content

I. Mathematical Methods:

This section includes two modeling techniques: system identification (ID) models and physiological models. Figs. S1, S3 are schematics for the two techniques respectively; Fig. S2 shows HR response to both workload and ventilation; Fig. S4 shows results of the nonlinear optimal control for the static first principle model; and Fig. S5 shows HR response using the dynamic first principle model for the highest workload demand in Fig. 1.

II. Simulation Results for all Experimental Subjects:

Figs.S6-S20 show simulation results of applying the two techniques to the five subjects' data.

III. Nonlinear Dynamic Models from System ID:

A global nonlinear model is fit to explain the overall response of HR to a broad range of power generation. Fig. S21 shows the simulation result.

IV. Cross Validation:

Figs.S22-S23 and Table S1 show cross validation results for linear system identification; Fig. S24 shows cross validation results for the physiological modeling; Figs. S25-S26 shows cross validation results for the nonlinear system identification.

V. Tables S2-S4:

Tables S2-S4 provide the necessary parameter values in the simulation.

VI. System Identification Techniques:

A pure technical introduction on system identification is provided.

Supporting Information

I. Mathematical Methods

1. System Identification Model

System identification begins with measurements of the behavior (output) of the system when external influences are imposed (i.e. inputs to the system), and then determines a mathematical model for this interaction without going into the details of what is actually happening inside the system. Though there exist many sophisticated numerical methods to identify a linear time invariant (LTI) dynamic system in order to fit observed input-output data, in general, it is difficult to mathematically characterize a complicated dynamic system, e.g. nonlinear system or a high order system. To minimize the complexity of the requisite model and numerical methods, this paper mainly uses low order LTI models in observable canonical form [33]. However, the entire physiological body system is a complex and not necessarily linear system. Therefore we carefully designed the experiments to ensure that the LTI model can provide a good approximate to the true system for each experiment.

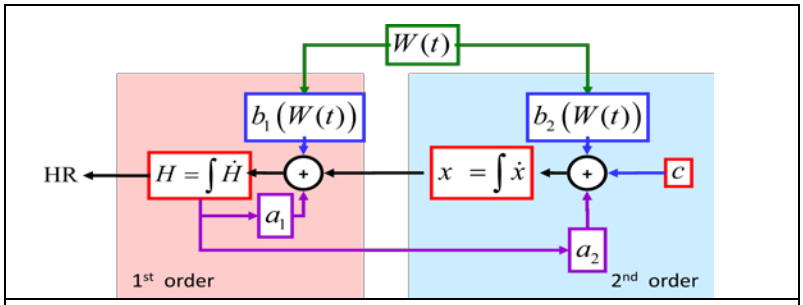

Figure S1: System Identification schematic

As an example, a 2nd order linear model in observable canonical form is shown as follow:

$$\begin{aligned} \Delta H(t) &= a_1 H(t) + b_1 W(t) + x(t) \\ \Delta x(t) &= a_2 x(t) + b_2 W(t) + c \end{aligned} \quad \text{(SI-1)}$$

where a_1, a_2, b_1, b_2, c are constants, W (workload power or ventilation) is the input signal, H (HR) is the output signal, and x is an internal state. In **Fig. 7**, we apply simple nonlinear models to fit the data for anaerobic exercise by using workload power as input. The nonlinear models have the same structure as (SI-1) except that $b_i \cdot W(t)$ is changed to be a piecewise linear function $b_i(W(t))$ in the form of (A schematic is shown in Fig. S1.):

$$b_i(W(t)) = \begin{cases} b_{i,1} \cdot W(t) & \text{if } W(t) \le 220 \text{ watts} \\ b_{i,2} \cdot W(t) & \text{else} \end{cases}$$

Given a certain order of this structure, we use nonlinear programming techniques [33] to search for parameter values that minimize the mean squared error between measured HR and simulated HR (H). We then iterate to find an order that gives a reasonable tradeoff between model complexity (order) and simulation error. Using observable canonical form reduces the search dimension of the nonlinear program without loss of generality. For readers unfamiliar with these methods, we provide a more technical introduction on system identification in SOM-Section VIII: *System Identification Techniques.*

We also use both workload W and ventilation V data as inputs to fit HR data during the easy workout in **Fig. 1**. Fig. S2 shows the output H (in black) of a simple 2-state, 7-parameter linear model with both W and V as inputs

$$\begin{aligned} \Delta H(t) &= a_1 H(t) + b_1 V(t) + d_1 W(t) + x(t) \\ \Delta x(t) &= a_2 x(t) + b_2 V(t) + d_2 W(t) + c \end{aligned}$$

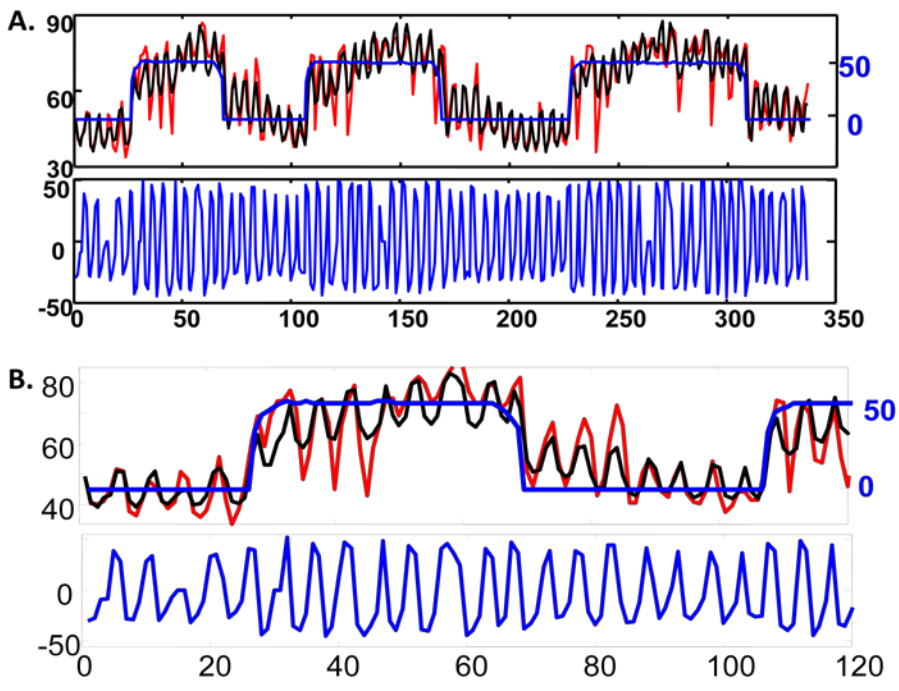

Figure S2: **HR response to both workload and ventilation: (A)** HR (red) and dynamic fit (black) to inputs of workload (blue in the top figure) and natural ventilation (blue in the lower figure); **(B)** is a zoomed in version of (A).

2. First Principle Model

In this section, we will focus on establishing the 1st principle model in Equation (2-4) and explain how we carried out the static and dynamic analysis (**Figs. 3-4**) using this physiological model.

The block diagram of the basic circulatory system is shown in Fig. S3 [32]. The basic task of the cardiovascular system is to satisfy metabolic requirement for O_2, glucose, and other nutrients while simultaneously removing CO_2 and the other end products of metabolism. To fulfill these tasks, the heart pumps blood through the pulmonary circuit and the systemic circuit. The heart consists of four chambers of two types: atria and ventricles. For simplicity, we will refer to the right atrium and right ventricle as the right heart, and the left atrium and left ventricle as the left heart. The left heart receives blood from the lungs which is rich in O_2, and pumps it into the systemic arteries distributing O_2 and metabolic substrates to end-organs. Metabolic end products are removed as O_2-depleted blood leaves the systemic peripheral tissues, enters the central venous compartment and returns to the right heart. The right heart pumps blood into the

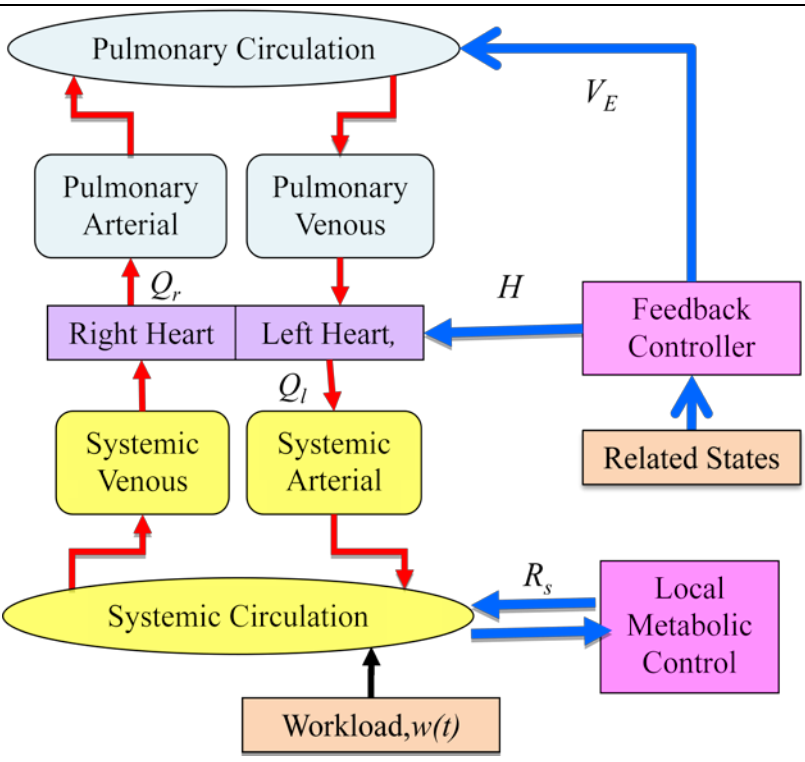

Figure S3: Block diagram of the basic cardiovascular model [32].

pulmonary arterial circulation, where O_2 is taken up from alveoli and CO_2 is transferred to alveoli and exhaled. Blood returns to the left heart via the pulmonary veins. The variables in the figure are explained in the following sections.

Our model is based on the circulatory circuit diagram, using standard mathematical descriptions of circulation, with a focus on modeling purely aerobic exercise. We only model blood flow and O_2 and we do not model CO_2, pH, glucose and other variables. CO_2 and pH are important signals, but during aerobic exercise in young, fit adults, changes in CO_2 correlate with changes in O_2 such that any signal that depends on CO_2 is approximately a function of O_2. Moreover, during short aerobic exercise, pH is almost constant. By modeling blood flow and O_2, the model captures the overall physiologic response during low level exercise in young, fit adults.

2.1 Basic Model

2.1.1 Blood Circulation Model

The circulation of blood is described by well-established models [27-32]. Here we build a simple model based on the models developed in Peskin *et al.* [31] and Batzel *et al.* [32] to explain cardiovascular control systems.

We distinguish four compartments of the circulatory system, i.e., the arterial and venous compartments of the systemic and pulmonary circuits, treating each compartment as a compliant vessel with no resistance to blood flow. That is, we assume that blood volume in the compartment is determined by pressure in the compartment. A simple linear relationship between pressure and volume in such a compartment is assumed:

$$\begin{aligned} V_{as} &= c_{as} P_{as} \\ V_{vs} &= c_{vs} P_{vs} \\ V_{ap} &= c_{ap} P_{ap} \\ V_{vp} &= c_{vp} P_{vp} \end{aligned}$$

V variables are volumes, P variables are pressures, and c is the compliance for a=arterial, v=venous, s=systemic, and p=pulmonary compartments.

The rate of change for the volume V in a compartment is the difference between the flow into and flow out of the compartment, described by the following equations:

$$\begin{aligned} c_{as}\dot{P}_{as} &= \dot{V}_{as} = Q_l - F_s \\ c_{vs}\dot{P}_{vs} &= \dot{V}_{vs} = F_s - Q_r \\ c_{ap}\dot{P}_{ap} &= \dot{V}_{ap} = Q_r - F_p \\ c_{vp}\dot{P}_{vp} &= \dot{V}_{vp} = F_p - Q_l \end{aligned} \qquad \text{(SI-2)}$$

Q variables are the cardiac outputs for l=left heart and r=right heart; F variables are the blood flow for s= systemic and p= pulmonary circulation. We will establish models for cardiovascular output Q and blood flow F in the following parts.

Cardiovascular output

Cardiac output is a function of heart rate (H) and stroke volume (V_{str}), the amount of blood pumped with each cardiac contraction:

$$Q_{co} = HV_{str} \qquad \text{(SI-3)}$$

and $V_{str} = V_{diast} - V_{syst} = c_{diast}P_v - c_{syst}P_a$.

Here we regard the ventricle as a compliance vessel in which compliance changes over time. V_{diast} is end-diastolic blood volume of the relaxed ventricle and V_{syst} is the end-systolic blood volume of the maximally contracted ventricle. P_a is the pressure in the arteries supplied by the ventricle and P_v is the pressure in the veins that fill it. Usually c_{syst} is very small and c_{diast} is much larger. A simple special case when $c_{syst} = 0$ yields a description of stroke volume:

$$V_{str} = c_{diast}P_v \qquad \text{(SI-4)}$$

Combining equations (SI-3) and (SI-4) describes cardiac output for the left and right heart respectively:

$$\begin{aligned} Q_r &= c_r \cdot H \cdot P_{vs} \\ Q_l &= c_l \cdot H \cdot P_{vp} \end{aligned} \qquad \text{(SI-5)}$$

c_r and c_l are c_{diast} for the right and left heart respectively.

Blood Flow in the Circulation

We assume that the systemic and pulmonary circulation acts like a pure resistance vessel to blood flow. By Ohm's law,

$$\begin{aligned} F_s &= (P_{as} - P_{vs}) / R_s \\ F_p &= (P_{ap} - P_{vp}) / R_p \end{aligned} \quad \text{(SI-6)}$$

where *R* variables represent resistance to blood flow.

In our model, we assume that the pulmonary resistance R_p is a constant parameter, while the peripheral resistance R_s is decreased during exercise and the decrease is determined by local metabolic control. The purpose of decreasing peripheral resistance in the arterioles is to increase blood flow and regional delivery of O_2, glucose, and other substrates as needed. With exercise, local dilation of the arterioles is triggered by local release of vasodilating factors. We assume that peripheral resistance R_s is determined as [31]:

$$R_s = A \cdot [O_2]_v + R_{s0} \quad \text{(SI-7)}$$

A and R_{s0} are two constants; and $[O_2]_v$ is the tissue oxygen content which will be introduced later.

Blood Pressure Model

Assuming a constant total blood volume V_{tot}:

$$V_{as} + V_{vs} + V_{ap} + V_{vp} = V_{tot} \quad \text{(SI-8)}$$

Combining equations (SI-2), (SI-5), (SI-6), (SI-8) yields the following dynamic blood circulation model:

$$\begin{aligned} c_{as}\dot{P}_{as} &= c_l \cdot H \cdot P_{vp} - \left(P_{as} - P_{vs}\right) / R_s \\ c_{vs}\dot{P}_{vs} &= \left(P_{as} - P_{vs}\right) / R_s - c_r \cdot H \cdot P_{vs} \\ c_{ap}\dot{P}_{ap} &= c_r \cdot H \cdot P_{vs} - \left(P_{ap} - P_{vp}\right) / R_p \\ c_{vp}P_{vp} &= V_{total} - \left(c_{as}P_{as} + c_{vs}P_{vs} + c_{ap}P_{ap}\right) \end{aligned} \quad \text{(SI-9)}$$

Note that the equation for P_{vp} is not a dynamic equation.

2.1.2 Tissue Oxygen Transport Model

The equation describing oxygen exchange in the tissue compartment is [29-32]:

$$v_{T,O_2}[\dot{O}_2]_T = -M + F_s([O_2]_a - [O_2]_v) \quad \text{(SI-10)}$$

The left hand side of the equation represents the change in O_2 content across the tissue compartment, which is calculated by multiplying the fixed effective O_2 volume v_{T,O_2} with the

change in O_2 content $[O_2]_T$. The right hand side of the equation describes the net volume changes in terms of the metabolic consumption of O_2 denoted by *M* and its supply described by the net change in the arterial and venous blood O_2 contents denoted, respectively, by $[O_2]_a$ and $[O_2]_v$.

We use the following empirical formula for the resulting metabolic rate *M*:

$$M = \rho \cdot W + M_0$$

where W is the ergometric workload imposed on the subject during exercise, M_0 is the metabolic rate in systemic tissue corresponding to zero workload and ρ is a positive constant parameter. Moreover, we assume that tissues and venous blood gases are in equilibrium; tissue oxygenation $[O_2]_T$ is the same as venous oxygenation $[O_2]_v$, i.e.

$$[O_2]_T = [O_2]_v$$

2.1.3 The Basic Model

Equations (SI-9), (SI-10) are combined to be the first principle model with 4 states and 1 unknown controllers:

$$\begin{aligned}
c_{as}\dot{P}_{as} &= c_l \cdot H \cdot P_{vp} - (P_{as} - P_{vs}) / R_S \\
c_{vs}\dot{P}_{vs} &= \left(P_{as} - P_{vs}\right) / R_S - c_r \cdot H \cdot P_{vs} \\
c_{ap}\dot{P}_{ap} &= c_r \cdot H \cdot P_{vs} - (P_{ap} - P_{vp}) / R_p \\
v_{T,O_2}[\dot{O}_2]_v &= -(\rho \cdot W + M_0) + F_s \cdot \left(\left[O_2\right]_a - \left[O_2\right]_v\right) \qquad \text{(SI-11)} \\
c_{vp}P_{vp} &= V_{total} - \left(c_{as}P_{as} + c_{vs}P_{vs} + c_{ap}P_{ap}\right) \\
R_s &= A \cdot [O_2]_T + R_{s0} \\
H &= u(\cdot)
\end{aligned}$$

where $u(\bullet)$ is the control function of heart rate *H*. The model describes a 4-state nonlinear dynamic system (again, note that the equations for P_{vp} and R_s are not dynamic equations.). We will describe how to determine the control function below.

2.2 Control Mechanisms

The cardiovascular control system is complex and has been studied intensively [27, 28, 32], but unresolved questions and controversies about HR control and HRV persist. Homeostasis is manifested in healthy physiological states, meaning that steady state behavior is maintained despite varying inputs to the system [4, 5, 27, 28, 32]. The physiologic response to perturbations

(such as exercise in our study) reveals the dynamic behavior of the control systems that maintain homeostasis.

Exercise is an important physiologic perturbation. The control objective of normal physiology is to produce sufficient energy for muscle activity, while maintaining critical biologic parameters within an acceptable range. Ventilation, vascular resistance, and blood flow are the primary factors that govern operation of the cardiopulmonary system, maintaining a tradeoff between energy production requirements and physiological equilibrium. In order to deliver sufficient O_2 during exercise, ventilation increases, cardiac output rises and skeletal muscle arterioles dilate. The magnitude of these responses is bounded in order to remain acceptable close to equilibrium. The degree to which they are bounded highlights how the cardiopulmonary system manages this tradeoff. Critical physiologic variables must be controlled so that actual structural damage is prevented [27, 28, 32]. The arterial partial pressure of oxygen, P_{a,O_2}, is the key regulated variable with a set-point of ~100 mm Hg. As a result of this tight control on P_{a,O_2}, the hemoglobin in systemic arterial blood is kept saturated with oxygen yielding (in the absence of anemia) a systemic arterial oxygen content $[O_2]_a$ of around 20 ml O_2/100 ml blood. This is demonstrated by the nearly constant SpO_2 value which is maintained during exercise, an observation supported both by the literature and our experimental data. In addition, the arterial partial pressure P_{as} is controlled by the baroreceptor loop, a short-term feedback control mechanism.

The intent here is not to model the entire circulatory control system in detail. Instead, we focus on nervous system control over heart rate H to guarantee "sufficient oxygen" and maintain P_{as} at a certain level. Rather than model the control system in detail, we construct a feedback controller which regulates heart rate based on several important system state variables, e.g. blood pressure, oxygen saturation, energy reserve. Here, we assume that the objective of the cardiovascular control system is to stabilize/balance those important variables around their (pre-)defined/safe values as well as to minimize the work done by the heart. Thus the loop can be considered as a stabilizing and optimizing feedback. We will carry out steady state analysis first and then explain the dynamical cases.

Before carrying out the analysis, we simplify notations by defining the state vector:

$$s = (P_{as}, P_{vs}, P_{ap}, [O_2]_v)^T \in R^4$$

and the parameter vector,

$$p = (c_{as}, c_{vs}, c_{ap}, c_{vp}, c_l, c_r, V_{tot}, R_p, R_{s0}, [O_2]_a, A, \rho, M_0, V_{T,O_2})^T \in R^{14} \quad \text{(SI-12)}$$

Then the model (4-state nonlinear system) can be defined as:

$$\dot{s} = F(s(t), p, W, H)$$

In the following analysis, we shall not fit the parameter vector *p* in (SI-12), but instead, we take physiologic nominal values from the literature for all parameters *p,* which is shown in Table 2-3. For all experimental subjects, we use the same parameter values for *p* except for the two parameters of cardiac output, c_l and c_r . For these, we use larger values for the larger subjects. The parameters that we fit will be introduced later.

Static Analysis

To obtain a steady state model for the cardiovascular system, we set the right side of equation (11) to be 0, and solve for mean systemic arterial blood pressure and oxygen saturation as a function of heart rate and workload, (P_{as}, ΔO_2)=*f*(*H*,*W*), where P_{as} is the mean systemic arterial blood pressure and ΔO_2 is $[O_2]_a - [O_2]_T$:

$$\begin{aligned} P_{as} &= \frac{(V_{tot} + c_{as} \cdot M_{O_2} \cdot A) \cdot (1 + c_r \cdot A \cdot [O_2]_a \cdot H + c_r \cdot R_s \cdot H)}{c_r \cdot B + (c_{as} \cdot A \cdot [O_2]_a + c_{as} \cdot R_{s0} + c_{ap} \cdot R_p) \cdot c_r \cdot H} - A \cdot M_{O_2} \\ \Delta O_2 &= \frac{M}{V_{tot} + c_{as} \cdot M_{O_2} \cdot A} \cdot \left(c_{as} \cdot A \cdot [O_2]_a + c_{as} \cdot R_{s0} + c_{ap} \cdot R_p + B / H \right) \end{aligned} \quad \text{(SI-13)}$$

where $B = \frac{c_{as}}{c_r} + \frac{c_{vs}}{c_r} + \frac{c_{ap}}{c_l} + \frac{c_{vp}}{c_l}$. Using the two equations, we get the mesh plot in Fig 3.

As discussed above, we model the regulation on *H* as optimal feedback control to minimize the deviation of the important physiologic variables from normal resting values. Mathematically, the optimal *H* is solved by minimizing the following objective function:

$$\min \; q_P \left(P_{as} - P_{as}^* \right)^2 + q_{o_2} \left(\Delta O_2 - \Delta O_2^* \right)^2 + q_H \left(H - H^* \right)^2 \quad \text{(SI-14)}$$

Here q_P, q_{o_2}, q_H are weighting factors and $P_{as}^*, \Delta O_2^*, H^*$ are steady values for $P_{as}, \Delta O_2, H$ at the referenced workload level W^*.

To solve the optimization problem, we linearize the two equations in (SI-13) for P_{as}, ΔO_2 around the referenced point ($P_{as}^*, \Delta O_2^*, H^*, W^*$) and get the following two linear expressions for P_{as}, ΔO_2:

$$P_{as} - P_{as}^* = a_1 \cdot (H - H^*) + b_1 \cdot (W - W^*)$$
$$\Delta O_2 - \Delta O_2^* = a_2 \cdot (H - H^*) + b_2 \cdot (W - W^*)$$

Then given a tradeoff weighting vector $\left(q_P, q_{O_2}, q_H\right)$, we can solve the optimization problem (SI-14) and the result is in the form of $H - H^* = b_3 \cdot (W - W^*)$. By tuning the tradeoff weighting vector $\left(q_P, q_{O_2}, q_H\right)$, we are able to get a physiologically plausible solution which is shown as the solid line in **Fig. 3**. The tradeoff weighting vector $\left(q_P, q_{O_2}, q_H\right)$ is set as follows:

- W=0~110watts: q_P =3, q_{O_2} =10^7, q_H =3;
- W=110~250watts: q_P =6, q_{O_2} =10^7, q_H =6;

The different q values reflect different tradeoffs between P_{as}, O_2, and HR as workload increases.

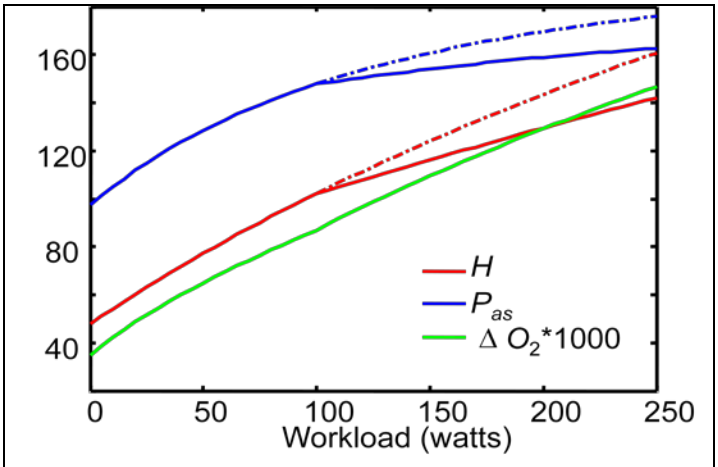

Figure S4: Nonlinear optimal control for static 1st principle model (HR: red; P_{as}: blue; ΔO_2 : green). Solid lines are the solutions by changing trade-off weight vectors between 0~110 watts and 110~250 watts. Dashed lines are the hypothetical solutions by using the same trade-off weight vectors for 110~250 watts as 0~110 watts.

We can also solve the optimization problem in (SI-14) without doing any linearization. Substituting (P_{as}, ΔO_2)=$f(H,W)$ in (SI-13) into the objection function in (SI-14), the optimization problem (SI-14) becomes a non-constrained optimization problem with the objective function in terms of H and W. Given the trade-off weighting vectors $\left(q_P, q_{O_2}, q_H\right)$, we can solve the optimization problem and find the optimal controller for H in terms of $h(W)$

which is a nonlinear function. By tuning the tradeoff weighting vector $\left(q_P, q_{O_2}, q_H\right)$, we are able to get a physiologically plausible solution which is shown in Fig. S4. The tradeoff weighting vector $\left(q_P, q_{O_2}, q_H\right)$ is set as follows:

- W=0~110watts: q_P =2, q_{O_2} =10^7, q_H =1.5;
- W=110~250watts: q_P =4, q_{O_2} =10^7, q_H =4;

Notice that we do not fit parameter vector p in (SI-12), but instead we just tune the tradeoff weighting vector. This means the model is over-determined and we require few parameters to fit the data, consistent with our findings based on system identification techniques. Fitting the tradeoff weighting vector in cost function ensures appropriate input-output behavior and has a physiologically plausible interpretation since it can determine how much each individual physiological term influences the cardiovascular control system.

Dynamic Analysis

Next, we determine the controller *u(.)* in the dynamic model (SI-11). Here, we assume that the objective of the cardiovascular control system is to quickly and sufficiently stabilize important physiologic variables to (pre-)defined/safe levels. Mathematically this can be obtained by minimizing the following cost function:

$$J(u(\cdot)) = \int_0^\infty \left(q_P^2 \left(P_{as}(t) - P_{as}^* \right)^2 + q_{O_2}^2 \left(\Delta O_2 - \Delta O_2^* \right)^2 + q_H^2 \left(H - H^* \right)^2 \right) dt \quad \text{(SI-15)}$$

Here q_P, q_{o_2}, q_H are weighting factors and $P_{as}^*, \Delta O_2^*, H^*$ are steady values for $P_{as}, \Delta O_2, H$ at the referenced workload level W^*.

In each interval exercise experiment shown in Fig. 4, there are two exercise levels. For each interval test, there is a steady state value s^* corresponding to the lower level workload. We introduce the transformation $\xi(t)$=$s(t)$-s^* and linearize the model (SI-11) around $\xi = 0$:

$$\dot{\xi}(t) = A\xi(t) + B(H(t) - H^*), \qquad t \geq 0$$
$$\xi(0) = s(0) - s^*,$$

where

$$A = \left.\frac{\partial F(s, p, W, H)}{\partial s}\right|_{s=s^*, W=W^*, H=H^*}$$

$$B = \left.\frac{\partial F(s, p, W, H)}{\partial H}\right|_{s=s^*, W=W^*, H=H^*}$$

H^* and W^* are corresponding heart rate and workload for the lower exercise level in each interval exercise test, which is 0 watts and 100 watts in our case.

Defining $C = (q_P, 0, 0, q_{O_2})$, the cost function (SI-15) takes on the form:

$$J(u(\cdot)) = \int_0^\infty \left(C\xi(t)\right)^2 + \left(q_H \hat{u}(t)\right)^2 dt$$

where $\hat{u}(t) = H(t) - H^*$. From control theory [34], the solution of this linear-quadratic regulator problem is given by a linear feedback law (*32*):

$$\hat{u}(t) = -K\xi(t),$$

where K is given by:

$$K = q_H^{-1} B^T P$$

and P is found by solving the continuous time algebraic Ricaati equation

$$A^T P + PA - PBq_H^{-1} B^T P + C^T C = 0$$

Therefore we obtain the controller on heart rate H in the following form:

$$H(t) = u(t) = \hat{u}(t) + H^l = -K\xi(t) + H^l.$$

As we do in static analysis, we fit the weighting vector q_P, q_{o_2}, q_H instead of fitting the parameter vector p to get the simulation results shown in Fig. 4. For different interval exercises, we have different q values. Those q values for different interval exercises reflect different tradeoffs between P_{as}, O_2, H, as their means increase. For each subject, those q values are shown in Table 4 and the corresponding simulation results are shown in SOM-Section II: *Simulation Results for all Experimental Subjects*.

However, if we apply this 1st principle aerobic model for the highest interval test in **Fig. 1**, the best simulation results we can obtain by tuning the weighting vector q is shown in Fig. S5, from which we can see that our aerobic model fails to capture most HR dynamics for anaerobic exercise.

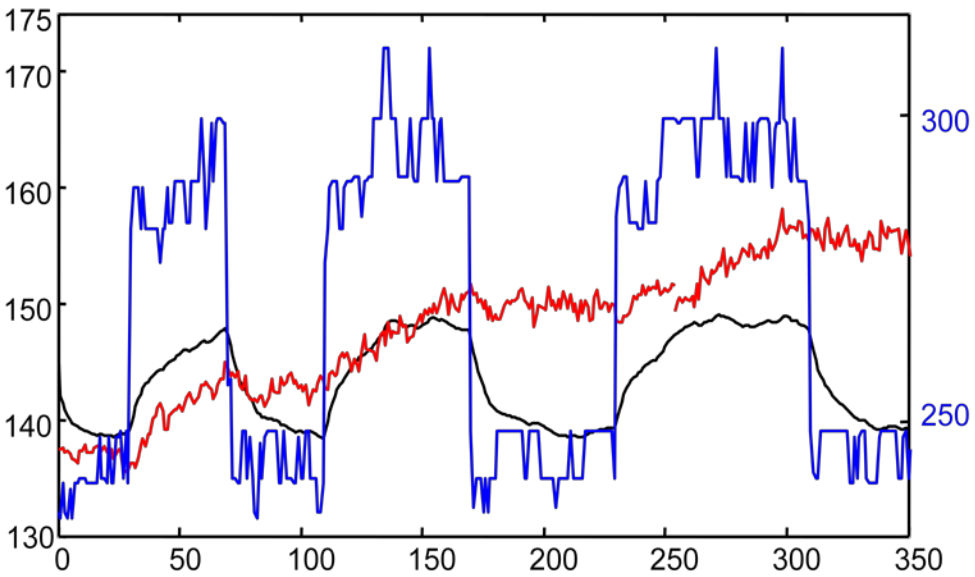

Figure S5: **HR response using 1st principle model for the highest workload (blue) demand in Fig. 1**. A physiological model with optimal controller is simulated with workload as input (blue) and HR (black) as output, and compared with collected HR data (red).

II. Simulation Results for all Experimental Subjects

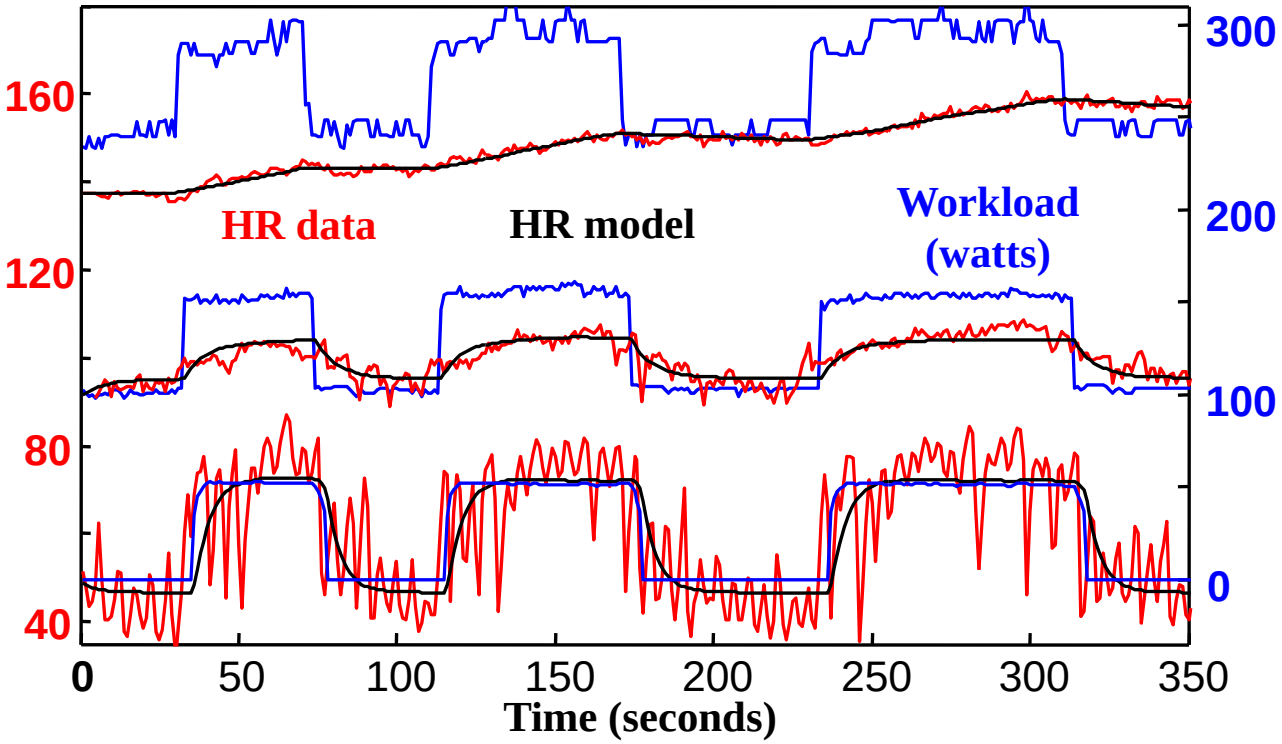

Figure S6: Subject #1 performed three separate experiments of less than 6 minutes each on a cycle ergometer. HR (left axis, red) is plotted for three different workload demands (right axis, blue). The workload profiles are similar but shifted square waves of 0-50 watts (lower), 100-150 watts (middle), and 250-300 watts (upper). A one state linear dynamic ("black box") model with 3 parameters (different for each case) was fit using workload input and HR output. The optimal parameter values (a, b, c)≈ (-0.22, 0.11, 10.2) at 0 watts differ greatly from those at 100 watts (-0.06, 0.012, 4.6) and at 250 watts (-0.003, 0.003, -0.27). Simulations of these 3 different models with the 3 corresponding workload inputs are in black. Breathing was spontaneous (not controlled), and SpO_2 was essentially constant throughout.

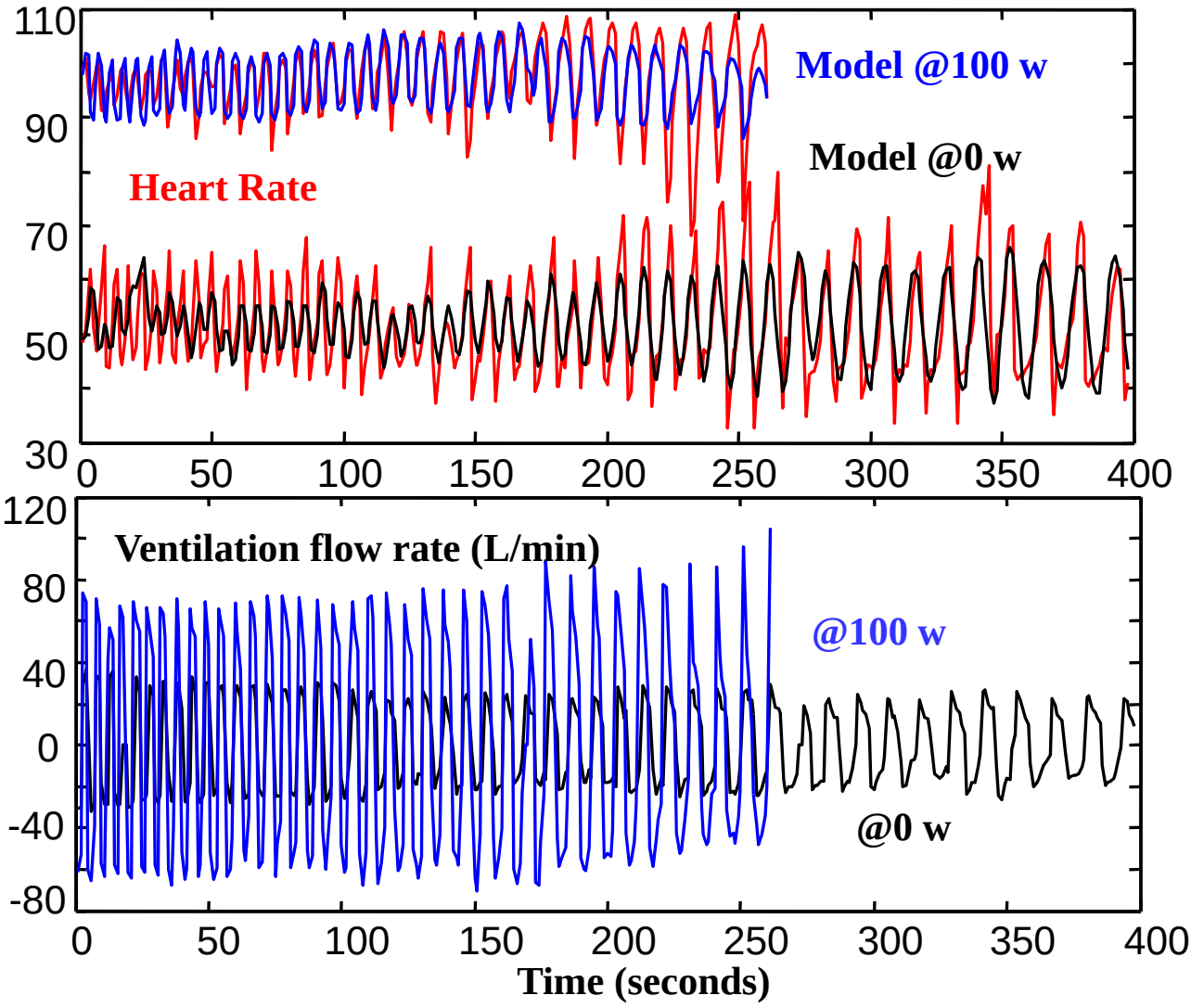

Figure S7: Subject #1's data: two experiments with input of controlled frequency sweeps in ventilation flow rate (lower plot) with fixed background workload demand of 0 watts (black) or 100 watts (blue). Subject #1 controlled breathing to follow a preprogrammed frequency sweep that spanned the natural breath frequencies at these workload levels. The ventilation data are raw speed of inhalation and exhalation at the mouthpiece. For each data set, a second order linear model was fit with airflow rate input (lower plot) and HR output (upper, data in red). Simulations of HR are in upper plot for 0 watts (black) and 100 watts (blue).

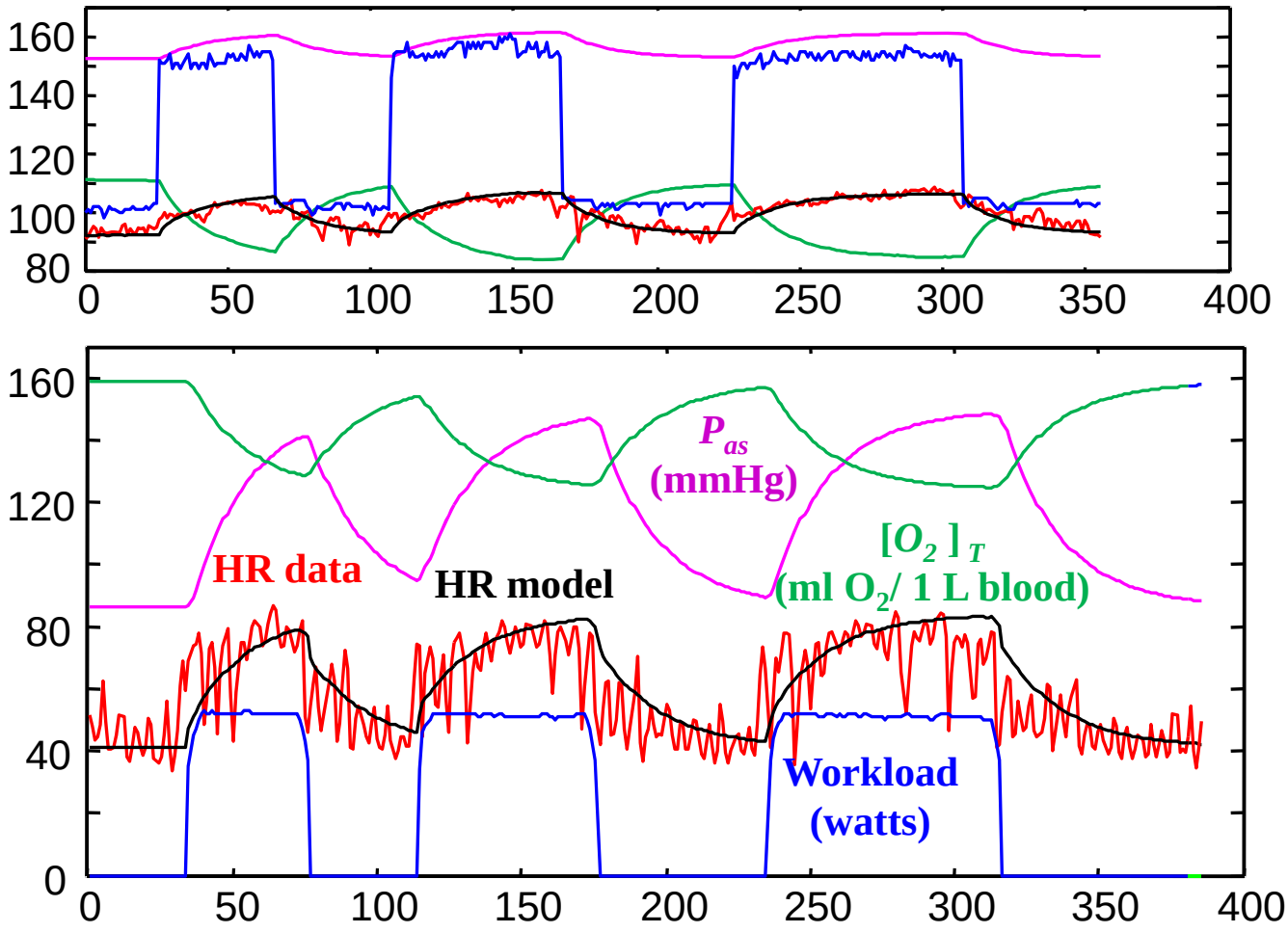

Figure S8: Subject #1's data: optimal control model of response to two different workload (blue) demands, approximately square waves of 0-50 watts (lower) and 100-150 watts (upper). For each data set, a first principle model with optimal controller is simulated with workload as input (blue) and HR (black) as output, which can be compared with HR data (red). Simulations of blood pressure (P_{as}, purple) and tissue oxygen saturation ($[O_2]_T$, green) are consistent with the literature but were not measured.

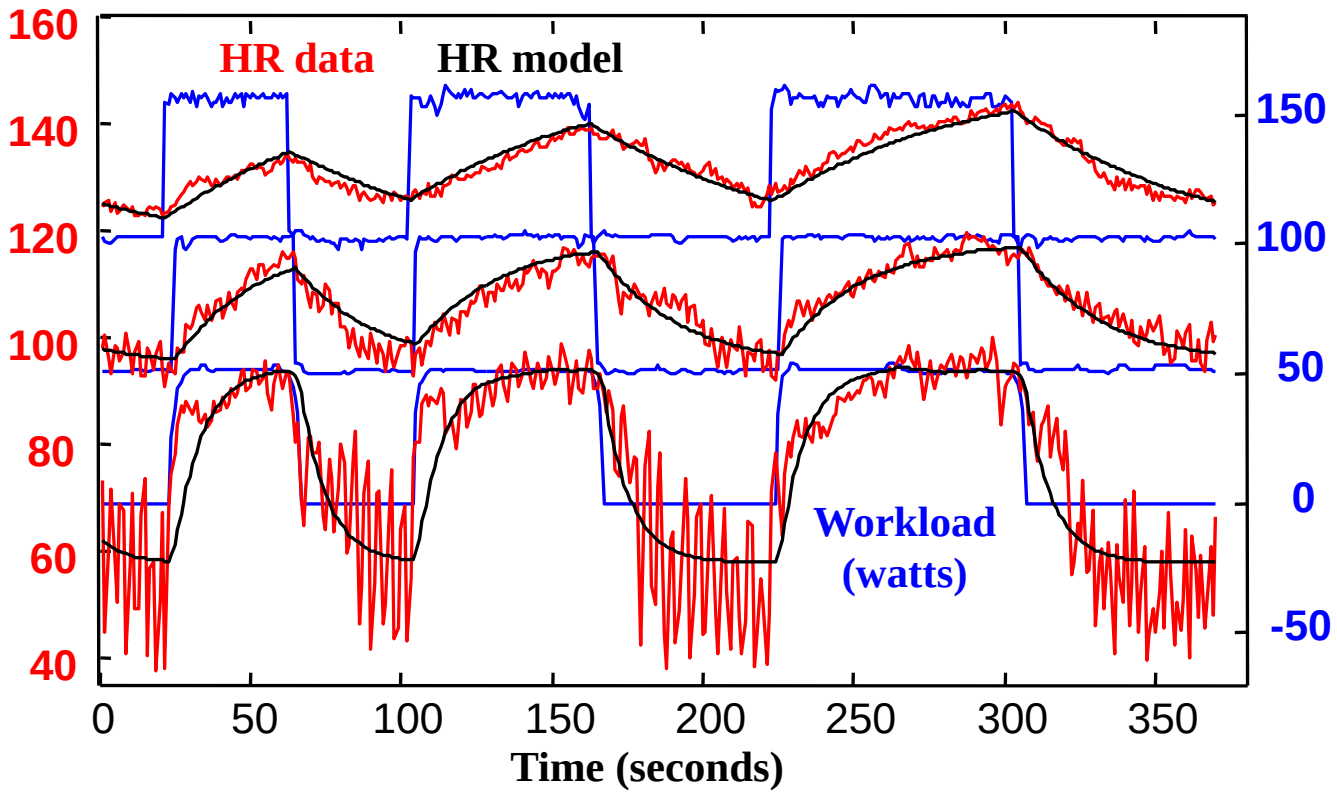

Figure S9: Subject #2 performed three separate experiments of less than 6 minutes each on a cycle ergometer. HR (left axis, red) is plotted for three different workload demands (right axis, blue). The workload profiles are similar but shifted square waves of 0-50 watts (lower), 50-100 watts (middle), and 100-150 watts (upper). A one state linear dynamic ("black box") model with 3 parameters (different for each case) was fit using workload input and HR output. The optimal parameter values (a, b, c)≈ (-0.11, 0.079, 6.54) at 0 watts differ greatly from those at 50 watts (-0.375, 0.017, 2.63) and at 100 watts (-0.014, 0.0095, 0.62). Simulations of these 3 different models with the 3 corresponding workload inputs are in black. Breathing was spontaneous (not controlled), and SpO_2 was essentially constant throughout.

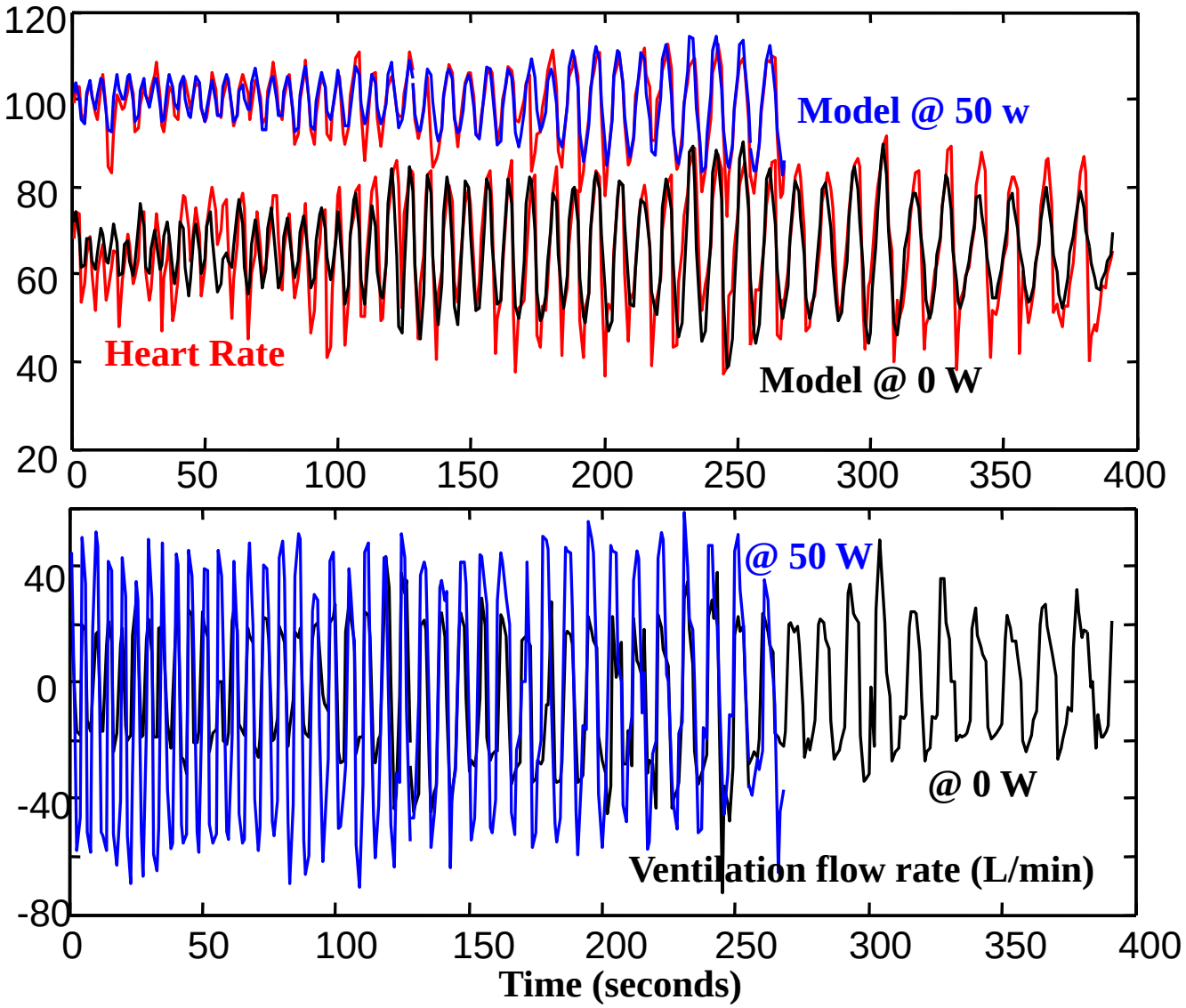

Figure S10: Subject #2's data: two experiments with input of controlled frequency sweeps in ventilation flow rate (lower plot) with fixed background workload demand of 0 watts (black) or 50 watts (blue). Subject #2 controlled breathing to follow a preprogrammed frequency sweep that spanned the natural breath frequencies at these workload levels. The ventilation data are raw speed of inhalation and exhalation at the mouthpiece. For each data set, a second order linear model was fit with airflow rate input (lower plot) and HR output (upper, data in red). Simulations of HR are in upper plot for 0 watts (black) and 50 watts (blue).

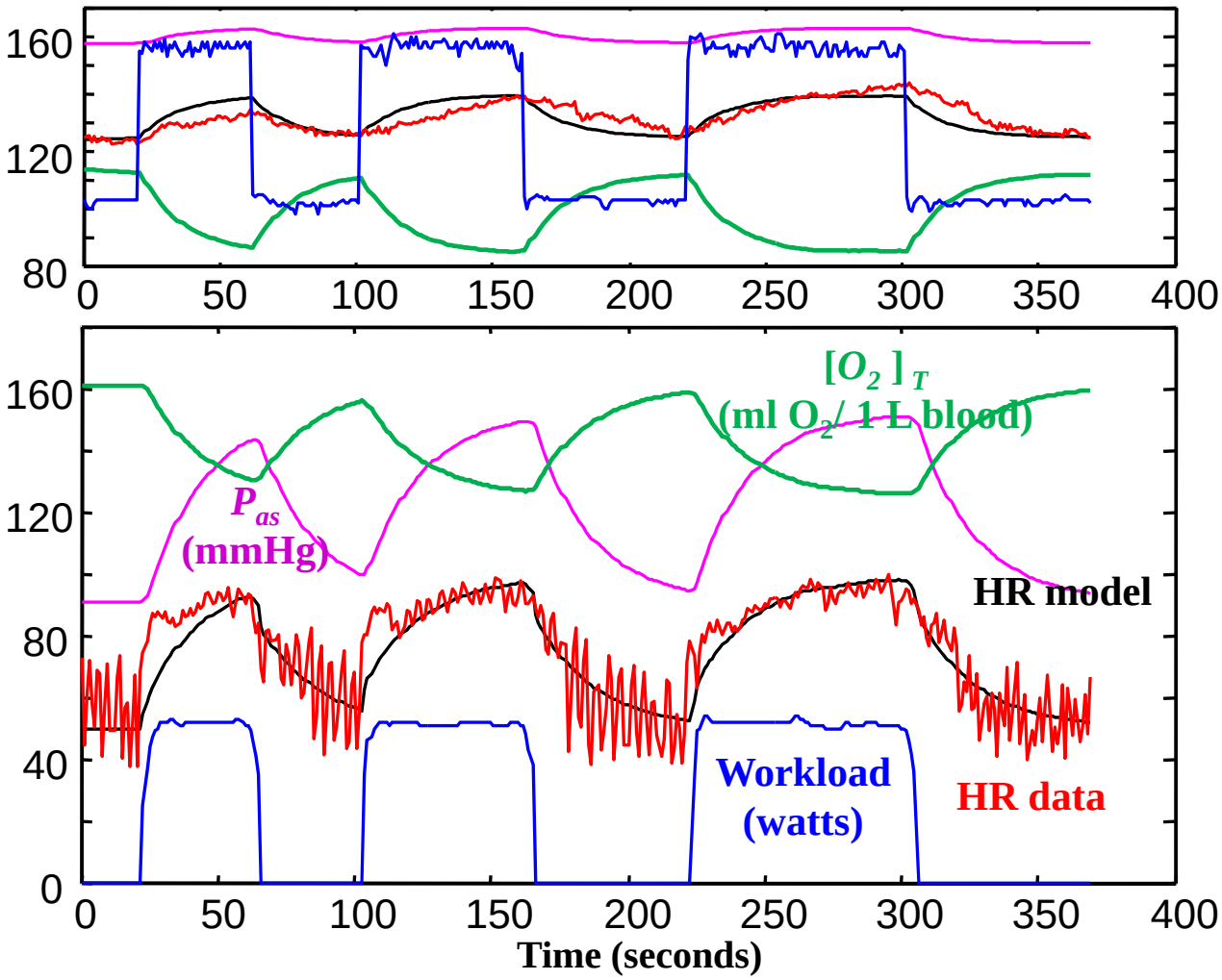

Figure S11: Subject #2's data: optimal control model of response to two different workload (blue) demands, approximately square waves of 0-50 watts(lower) and 100-150 watts (upper). For each data set, a first principle model with optimal controller is simulated with workload as input (blue) and HR (black) as output, which can be compared with HR data (red). Simulations of blood pressure (P_{as}, purple) and tissue oxygen saturation ($[O_2]_T$, green) are consistent with the literature but were not measured.

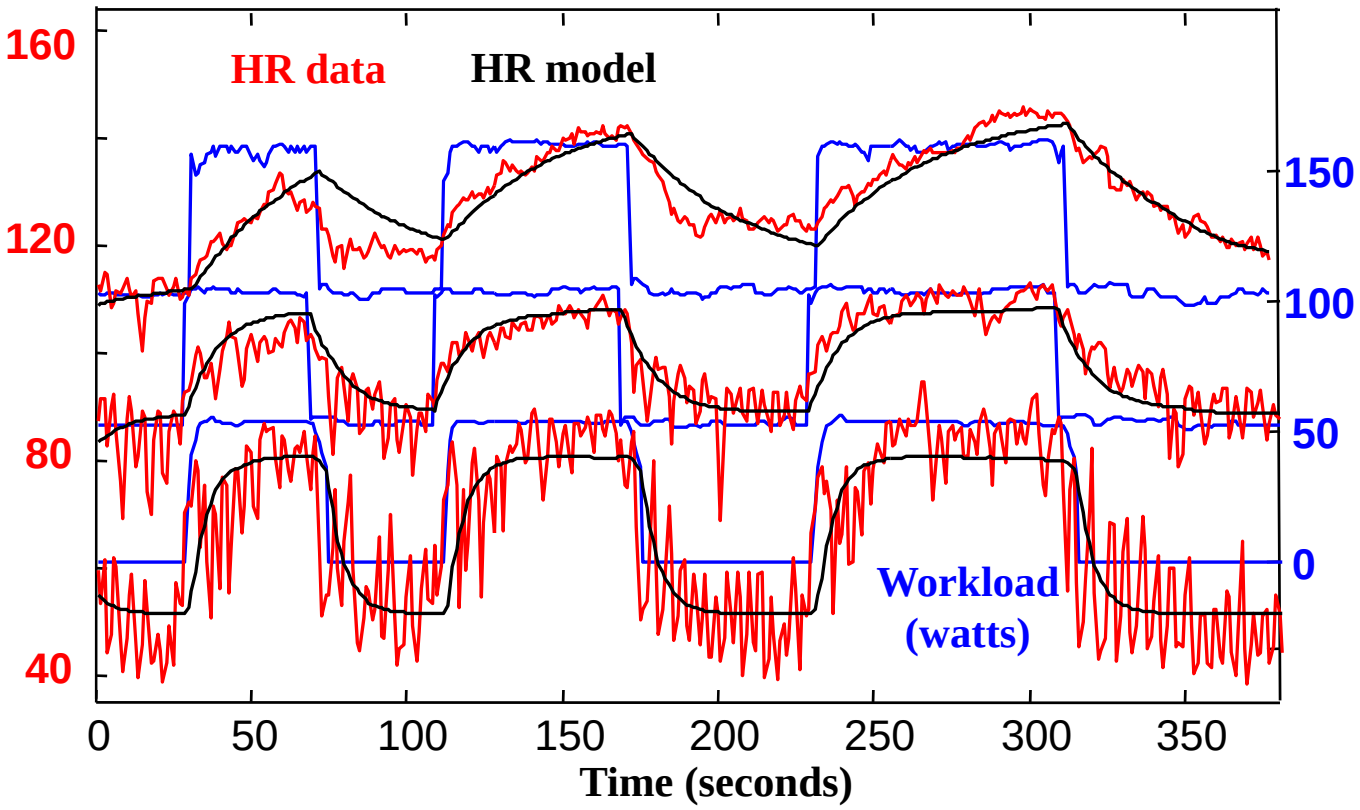

Figure S12: Subject #3 performed three separate experiments of less than 6 minutes each on a cycle ergometer. HR (left axis, red) is plotted for three different workload demands (right axis, blue). The workload profiles are similar but shifted square waves of 0-50 watts (lower), 50-100 watts (middle), and 100-150 watts (upper). A one state linear dynamic ("black box") model with 3 parameters (different for each case) was fit using workload input and HR output. The optimal parameter values (a, b, c)≈ (-0.18, 0.10, 9.47) at 0 watts differ greatly from those at 50 watts (-0.098, 0.037, 6.70) and at 100 watts (-0.028, 0.015, 1.59). Simulations of these 3 different models with the 3 corresponding workload inputs are in black. . Breathing was spontaneous (not controlled), and SpO_2 was essentially constant throughout.

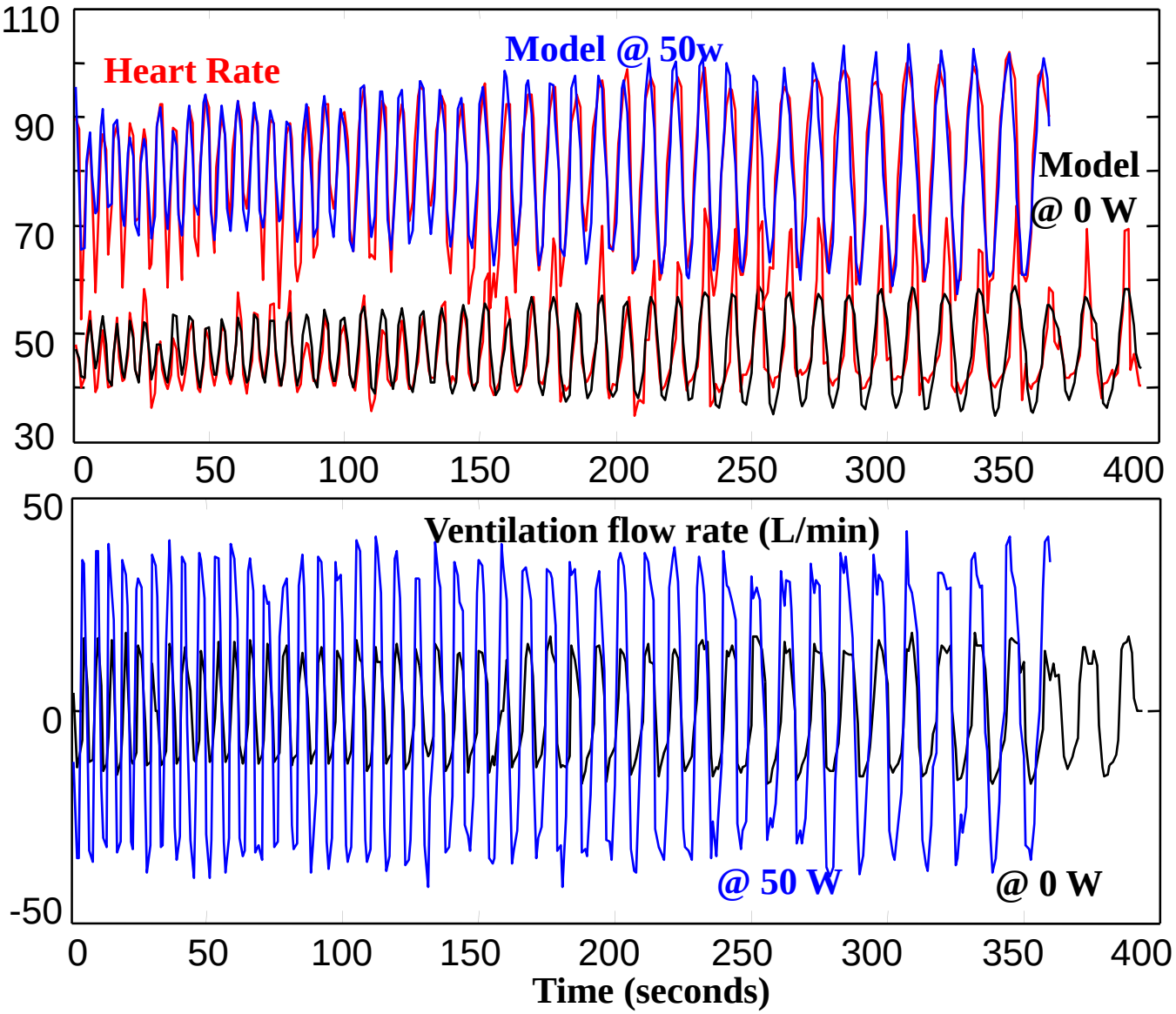

Figure S13: Subject #3's data: two experiments with input of controlled frequency sweeps in ventilation flow rate (lower plot) with fixed background workload demand of 0 watts (black) or 50 watts (blue). Subject #3 controlled breathing to follow a preprogrammed frequency sweep that spanned the natural breath frequencies at these workload levels. The ventilation data are raw speed of inhalation and exhalation at the mouthpiece. For each data set, a second order linear model was fit with airflow rate input (lower plot) and HR output (upper, data in red). Simulations of HR are in upper plot for 0 watts (black) and 50 watts (blue).

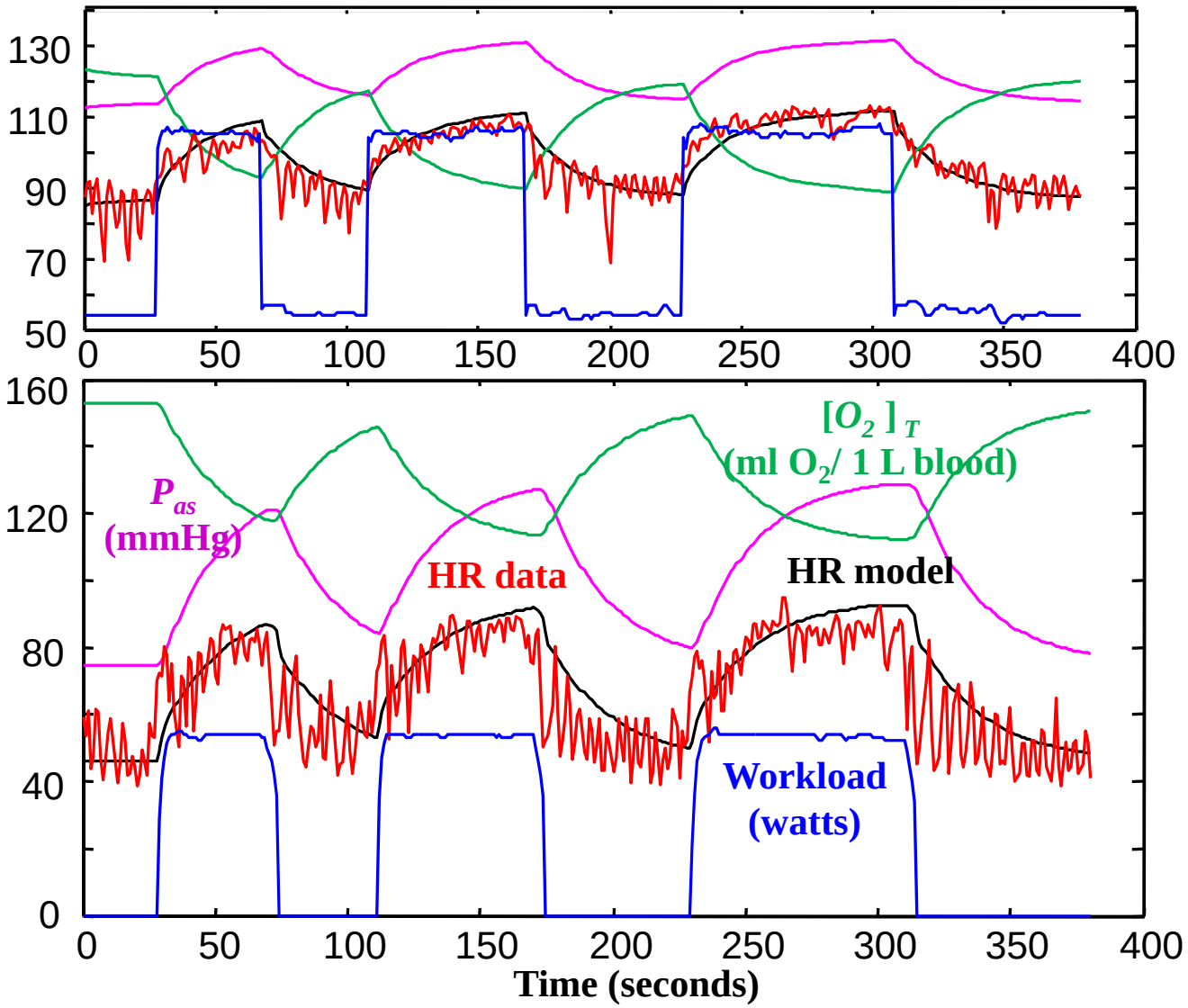

Figure S14: Subject #3's data: optimal control model of response to two different workload (blue) demands, approximately square waves of 0-50 watts (lower) and 50-100 watts (upper). For each data set, a first principle model with optimal controller is simulated with workload as input (blue) and HR (black) as output, which can be compared with HR data (red). Simulations of blood pressure (*BP*, purple) and tissue oxygen saturation ($[O_2]_T$, green) are consistent with the literature but were not measured.

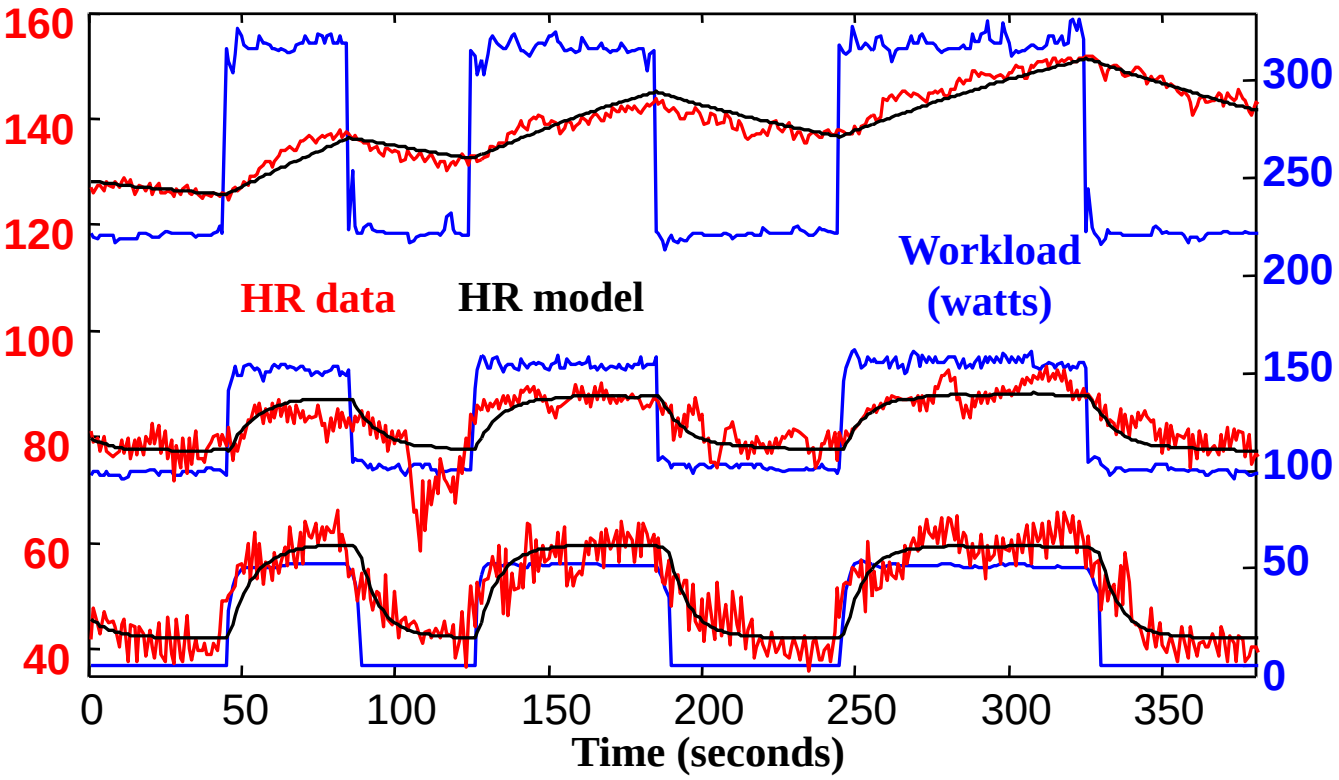

Figure S15: Subject #4 performed three separate experiments of less than 6 minutes each on a cycle ergometer. HR (left axis, red) is plotted for three different workload demands (right axis, blue). The watt profiles are similar but shifted square waves of 0-50 watts (lower), 100-150 watts (middle), and 220-320 watts (upper). A one state linear dynamic ("black box") model with 3 parameters (different for each case) was fit using watts input and HR output. The optimal parameter values (a, b, c)≈ (-0.15, 0.051, 6.41) at 0 watts differ greatly from those at 100 watts (-0.12, 0.023, 7.32) and at 220 watts (-0.0064, 0.0036, -0.039). Simulations of these 3 different models with the 3 corresponding workload inputs are in black. Breathing was spontaneous (not controlled), and SpO_2 was essentially constant throughout.

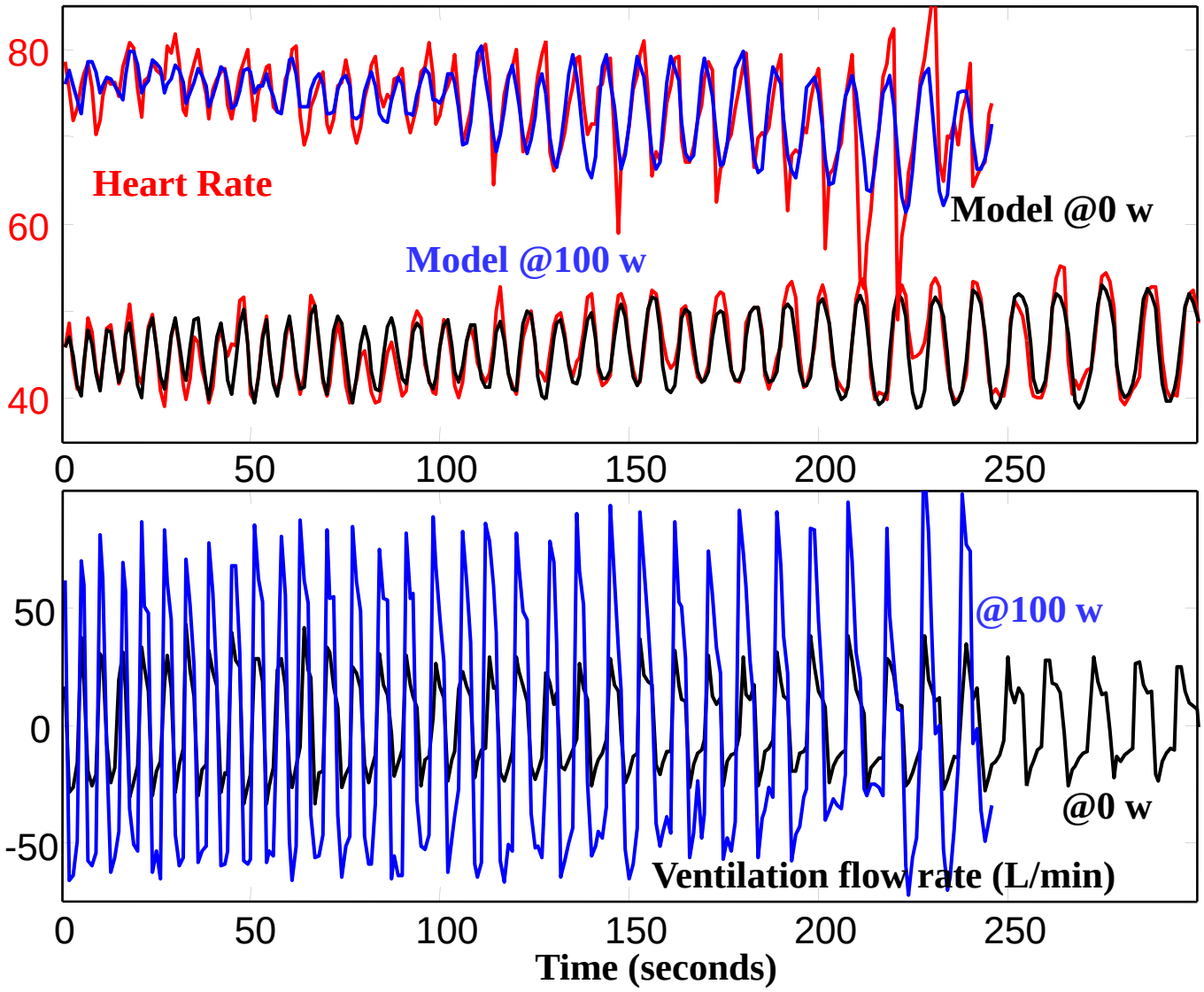

Figure S16: Subject #4's data: two experiments with input of controlled frequency sweeps in ventilation flow rate (lower plot) with fixed background workload demand of 0 watts (black) or 100 watts (blue). Subject #4 controlled breathing to follow a preprogrammed frequency sweep that spanned the natural breath frequencies at these workload levels. The ventilation data are raw speed of inhalation and exhalation at the mouthpiece. For each data set, a second order linear model was fit with airflow rate input (lower plot) and HR output (upper, data in red). Simulations of HR are in upper plot for 0 watts (black) and 100 watts (blue).

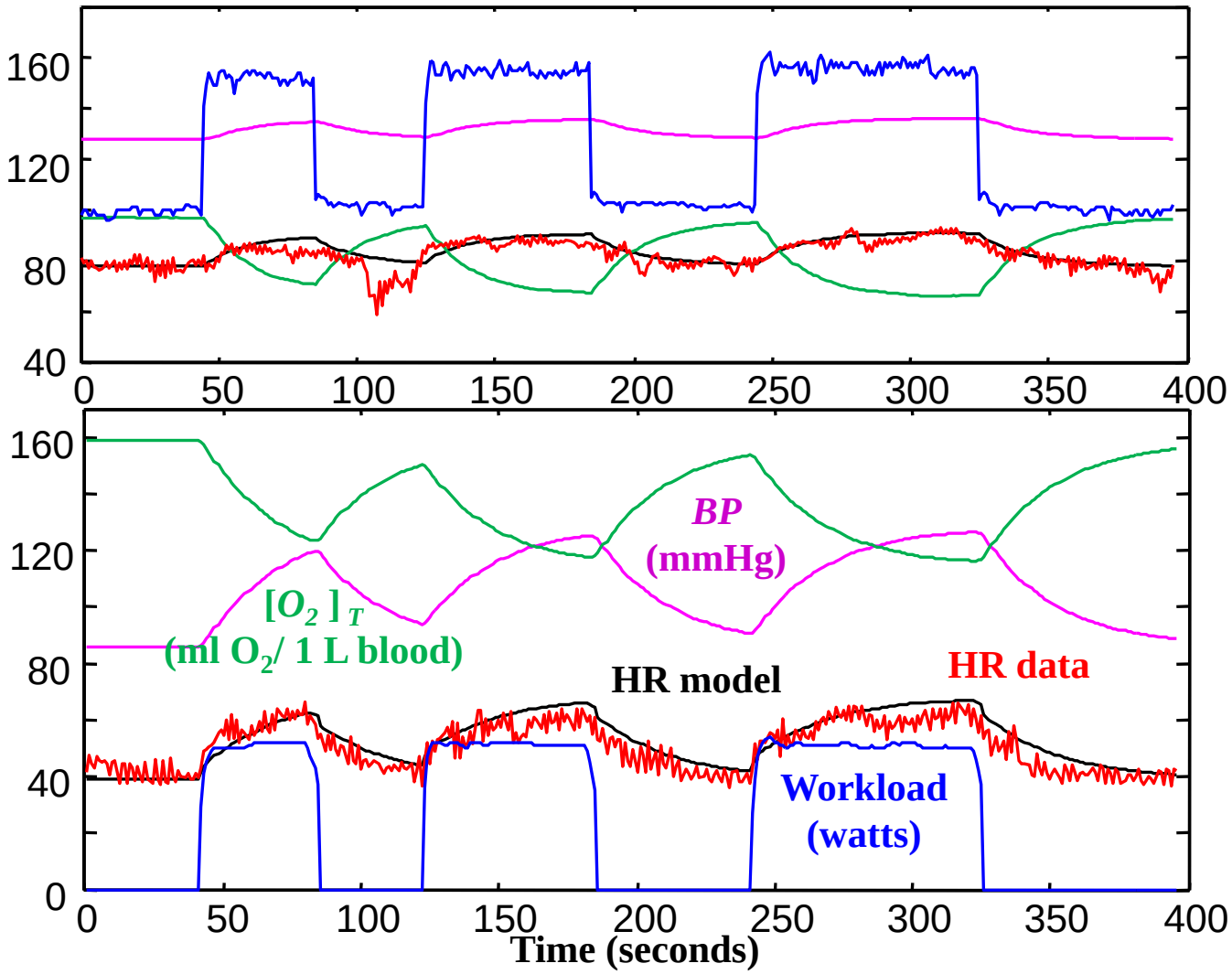

Figure S17: Subject #4's data: optimal control model of response to two different workload (blue) demands, approximately square waves of 0-50 watts (lower) and 100-150 watts (upper). For each data set, a first principle model with optimal controller is simulated with workload as input (blue) and HR (black) as output, which can be compared with HR data (red). Simulations of blood pressure (*BP*, purple) and tissue oxygen saturation ($[O_2]_T$, green) are consistent with the literature but were not measured.

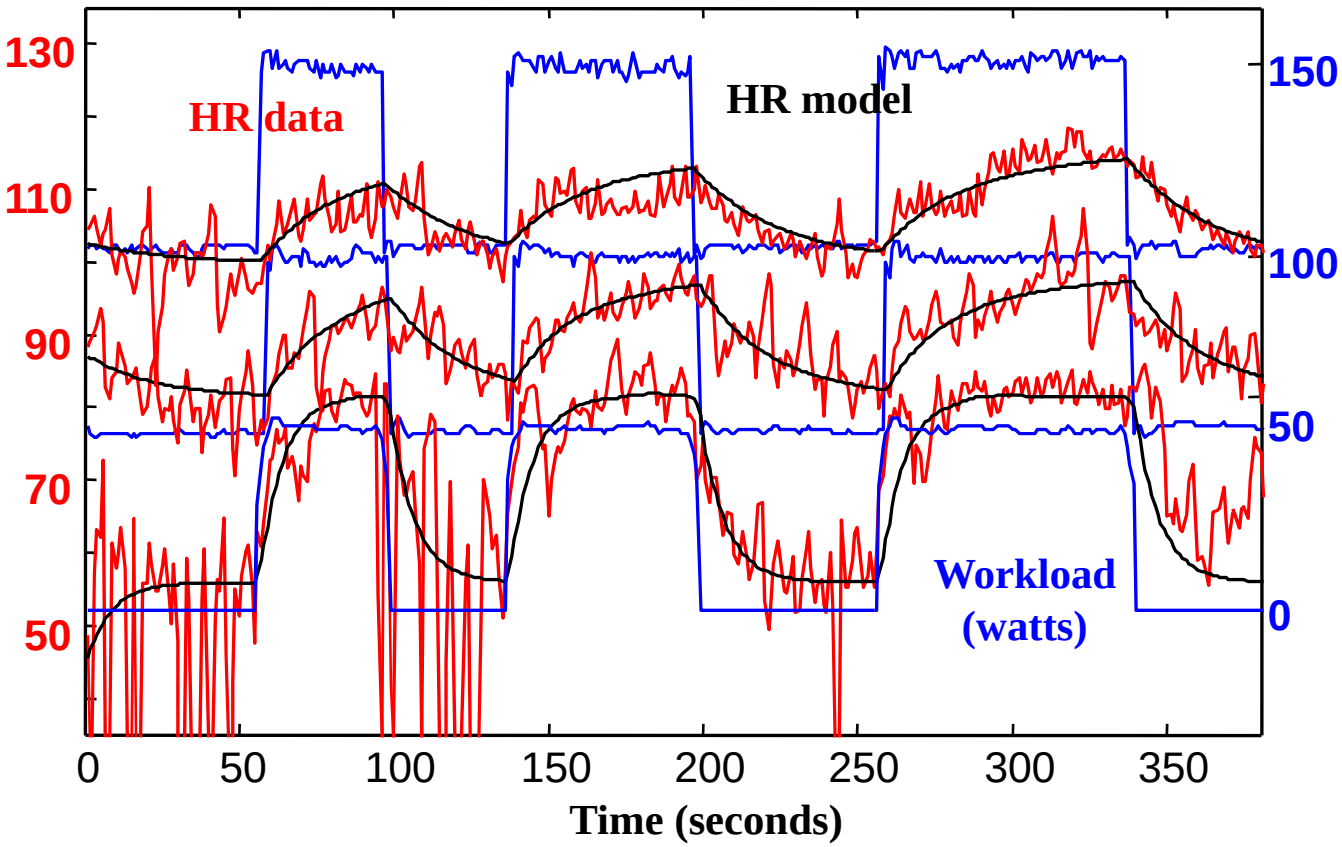

Figure S18: Subject #5 performed three separate experiments of less than 6 minutes each on a cycle ergometer. HR (left axis, red) is plotted for three different workload demands (right axis, blue). The workload profiles are similar but shifted square waves of 0-50 watts (lower), 50-100 watts (middle), and 100-150 watts (upper). A one state linear dynamic ("black box") model with 3 parameters (different for each case) was fit using workload input and HR output. The optimal parameter values (a, b, c)≈ (-0.13, 0.064, 7.05) at 0 watts differ greatly from those at 50 watts (-0.045, 0.015, 2.93) and at 100 watts (-0.036, 0.01, 2.54). Simulations of these 3 different models with the 3 corresponding workload inputs are in black. Breathing was spontaneous (not controlled), and SpO_2 was essentially constant throughout.

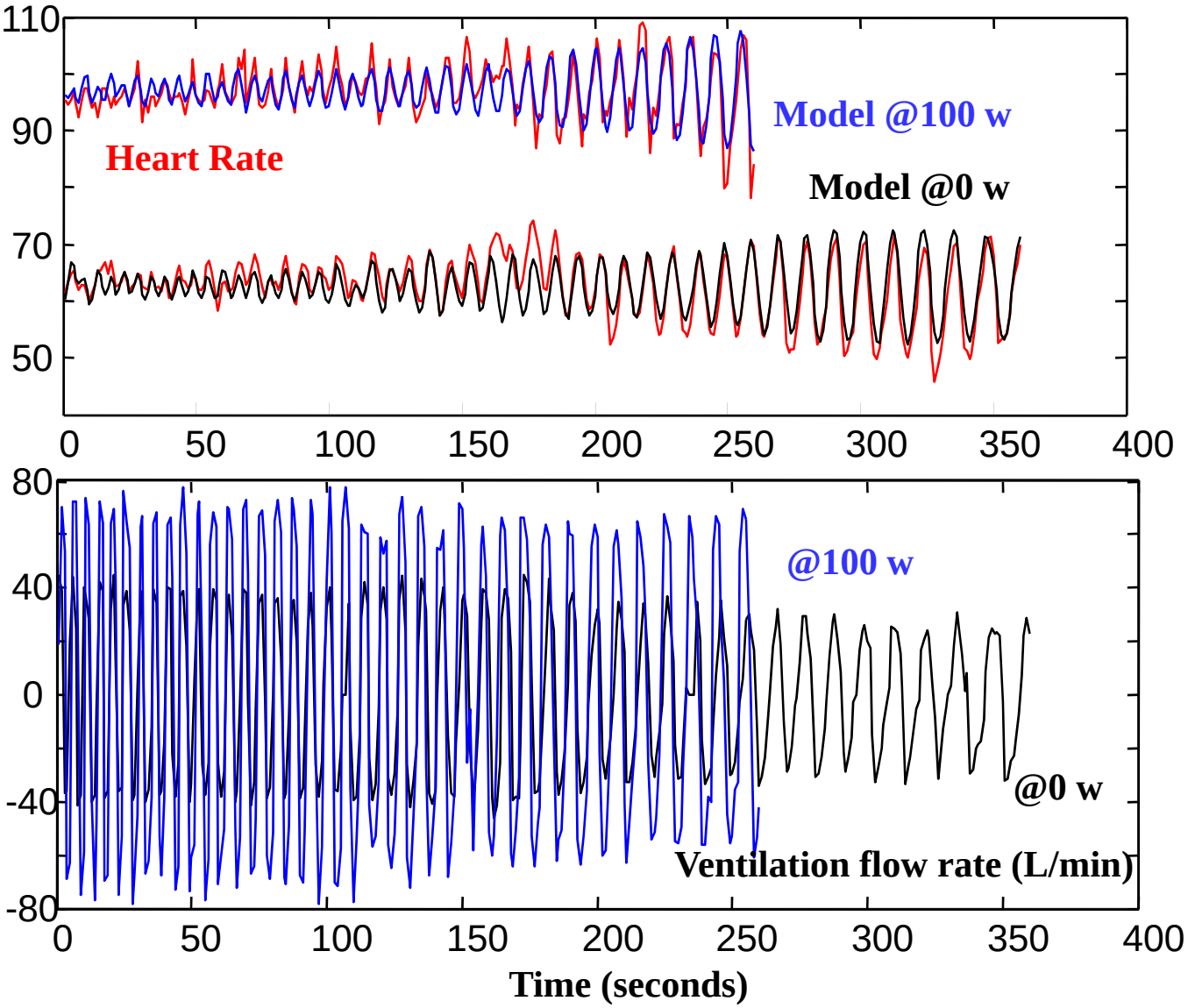

Figure S19: Subject #5's data: two experiments with input of controlled frequency sweeps in ventilation flow rate (lower plot) with fixed background workload demand of 0 watts (black) or 50 watts (blue). Subject #5 controlled breathing to follow a preprogrammed frequency sweep that spanned the natural breath frequencies at these workload levels. The ventilation data are raw speed of inhalation and exhalation at the mouthpiece. For each data set, a second order linear model was fit with airflow rate input (lower plot) and HR output (upper, data in red). Simulations of HR are in upper plot for 0 watts (black) and 50 watts (blue).

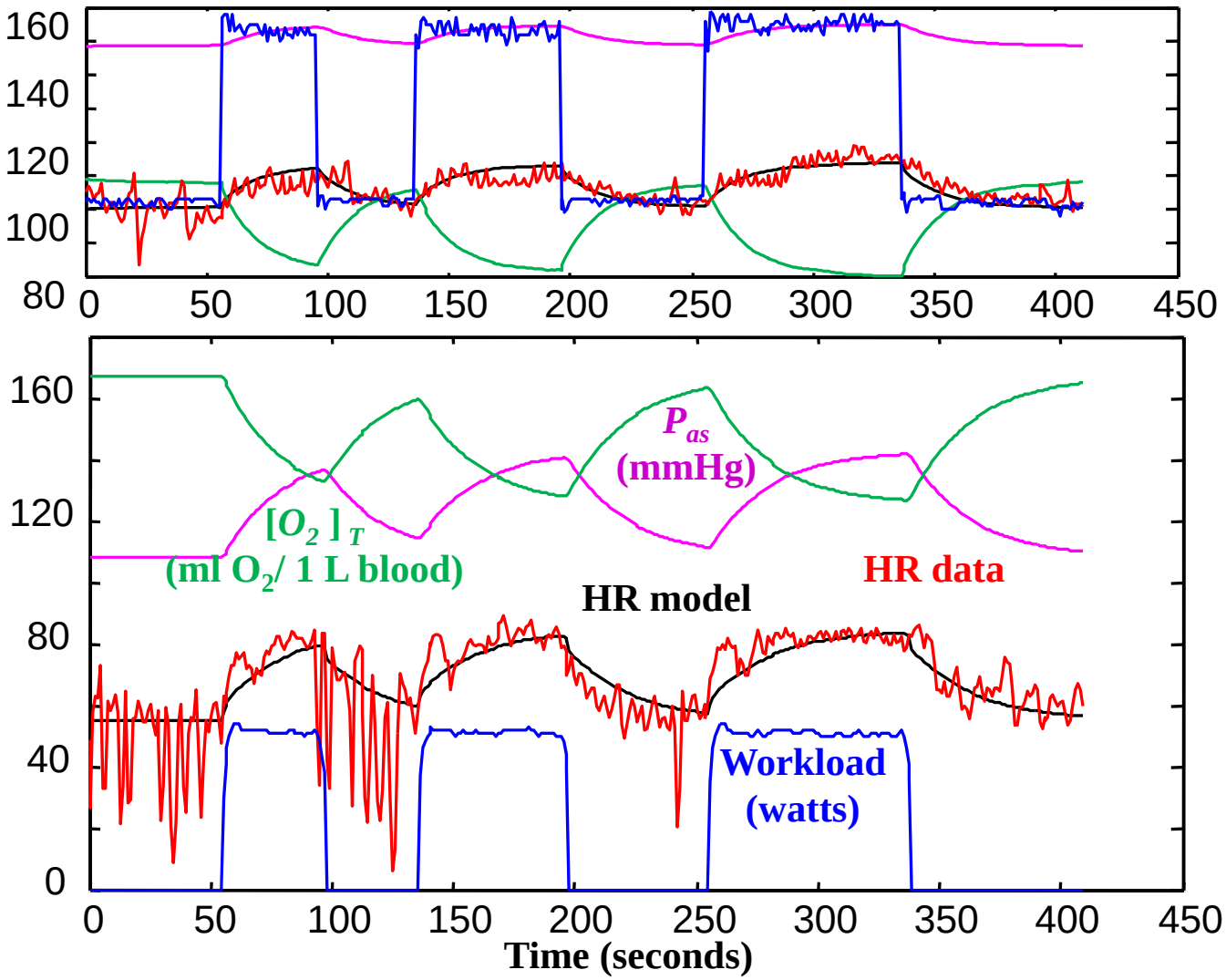

Figure S20: Subject #5's data: optimal control model of response to two different workload (blue) demands, approximately square waves of 0-50 watts (lower) and 100-150 watts (upper). For each data set, a first principle model with optimal controller is simulated with workload as input (blue) and HR (black) as output, which can be compared with HR data (red). Simulations of blood pressure (P_{as}, purple) and tissue oxygen content ($[O_2]_T$, green) are consistent with the literature but were not measured.

III. Nonlinear Dynamic Model from System ID

We have shown that overall HR response to a broad workload is a nonlinear system, by using experiments with limited watts range and individual but different linear models. To explore global nonlinear models, we did experiments including exercise levels between 0 watts and 150 watts and found a piecewise linear model to fit the data. The following two figures show two experiments data and the corresponding fitting results. In both of the fittings, we use piecewise 1st order linear model with 2 linear pieces and 7 parameters, which is shown as follows:

$$\begin{aligned} \Delta H(t) &= a_1 H(t) + b_1 W(t) + c_1; \quad \text{when } h(t) \le \bar{H} \\ \Delta H(t) &= a_2 H(t) + b_2 W(t) + c_2; \quad \text{otherwise} \end{aligned}$$

Constants $(a_1, b_1, c_1, a_2, b_2, c_2, \bar{H})$ are fitted to minimize the mean squared error between $H(t)$ and HR data. In SI-Section IV: *Cross Validation*, we show how validation results change with number of pieces and we claim that 2 linear pieces are an optimal balance between model order, fit, and cross validation. Wider watts ranges would require more states and nonlinearities.

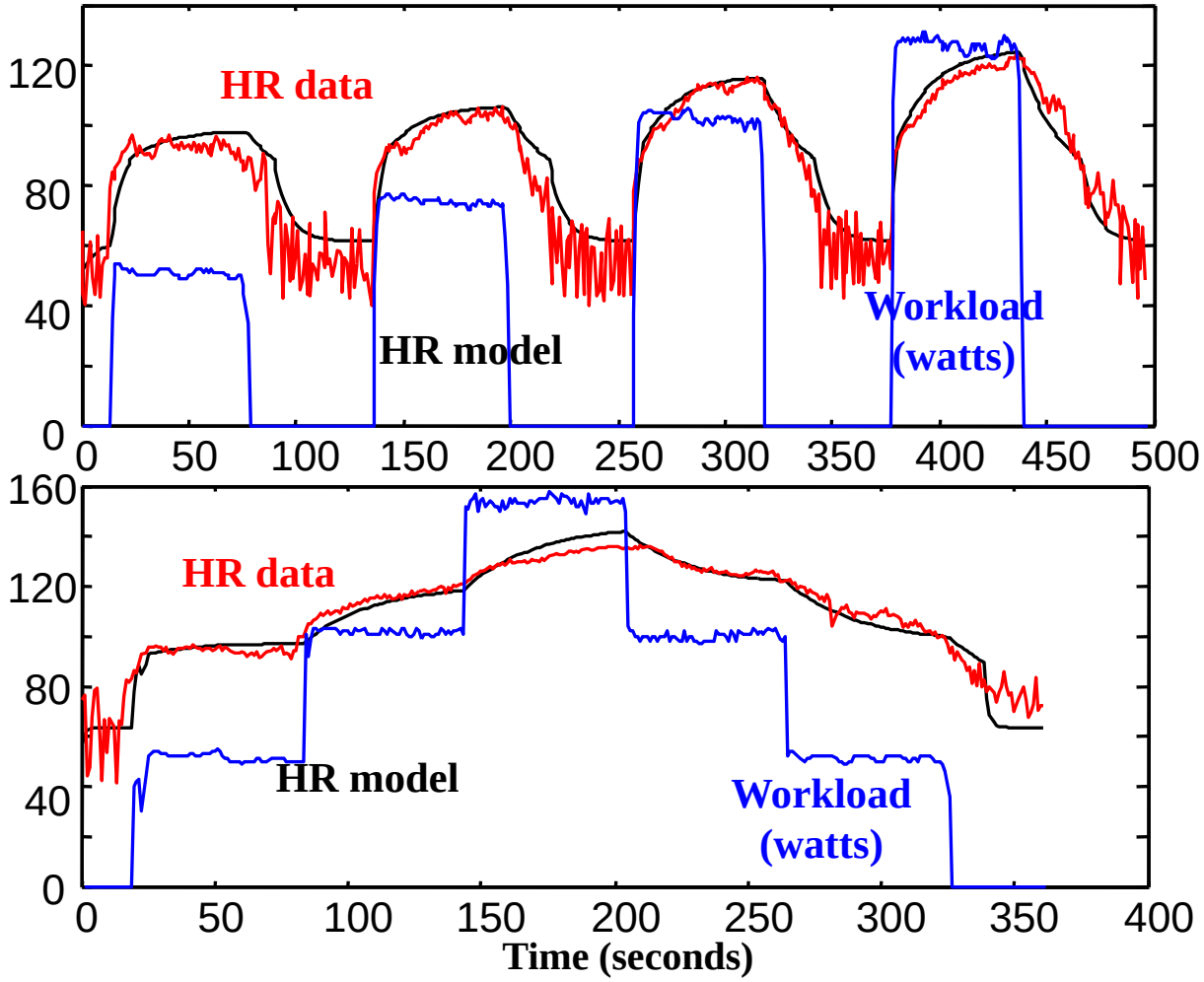

Figure S21: Subject #2 performed two separate experiments of less than 6 minutes each on a cycle ergometer. HR (left axis, red) is plotted for 2 different watts demands (blue) including exercise levels between 0 watts and 150 watts. For each experiments, a piecewise 1st order linear model ("black box") with 2 linear pieces and 7 parameters was fit using workload input and HR output. Simulations of this model with the 2 watts input are in black.

IV. Cross Validation

In this section, we perform cross validation on our models: the linear system identification model, the first principle model, and the nonlinear system identification model. In each cross validation, a subject performs two different exercise tests with different but comparable workload demands. We fit our models by using one set of experimental data (i.e. training data) and use the fitted models to perform prediction on the other set of experimental data (i.e. validation data). Moreover, in cross validation for linear system identification models and nonlinear system identification models, we fit and simulate different models with different complexities and we show how validation results correlate with the model complexities.

1. Linear System Identification Model

Fig. S22 shows an example of validation result for linear system identification models on two data sets. The subject performed two separate experiments of less than 8 minutes each on a cycle ergometer including exercise levels between 50 watts and 100 watts. We use the upper data set (called as data set 1) as training data and the lower data set (called as data set 2) as validation data. In Fig. S22, a 1st order linear dynamic ("black box") model (i.e., $\Delta h = ah + bW + c$) with 3 parameters (a,b,c) was fit using data set 1 with workload input and HR output and simulations of this model is done with the 2 workload inputs. From the simulation results, we can see that the 1st order linear dynamic model can predict HR response to workloads well.

To further address the over-fitting issue and to study how validation results correlate with model complexities, we then fit and simulate different models with different complexities on the two data sets. Fig. S23 and Table S1 shows the cross validation results. The classes of models we compare in the figure are: linear static model, 1st order linear dynamic model, 2nd order linear dynamic model, 3rd order linear dynamic model, and 4th order linear dynamic model. For each class of models, we do three different fittings: using data set 1 to fit a model; using data set 2 to fit a model; using both data set 1 and data 2 fit a model. Then we use those models to simulate both of the two data sets and calculate the corresponding root mean squared errors on those data sets. The root mean squared error is defined as:

$$\mathrm{RMS} = \sqrt{\frac{1}{N}\sum_{t=1}^{N}\left(H(t) - HR(t)\right)^2}$$

where $H(t)$ and $HR(t)$ are respectively the simulated and the measured heart rate at time point t, and N

is the total number of time points. The three markers in each line in Fig. S23 for each class of models show the simulated errors using the corresponding three different fitted models, which are, from left to right, the fitted model using data set 1, the fitted model using the two data sets; the fitted model using data set 2. Not surprisingly, Fig. S23 and Table S1 show that the RMS error becomes roughly smaller with increased fit complexity on the training data. However, the marginal benefit starts diminishing as the model complexity increases; moreover, the validation RMS error starts to increase if the model is very complex (see the RMS error for 3rd linear dynamic model and RMS error for 4th linear dynamic model).

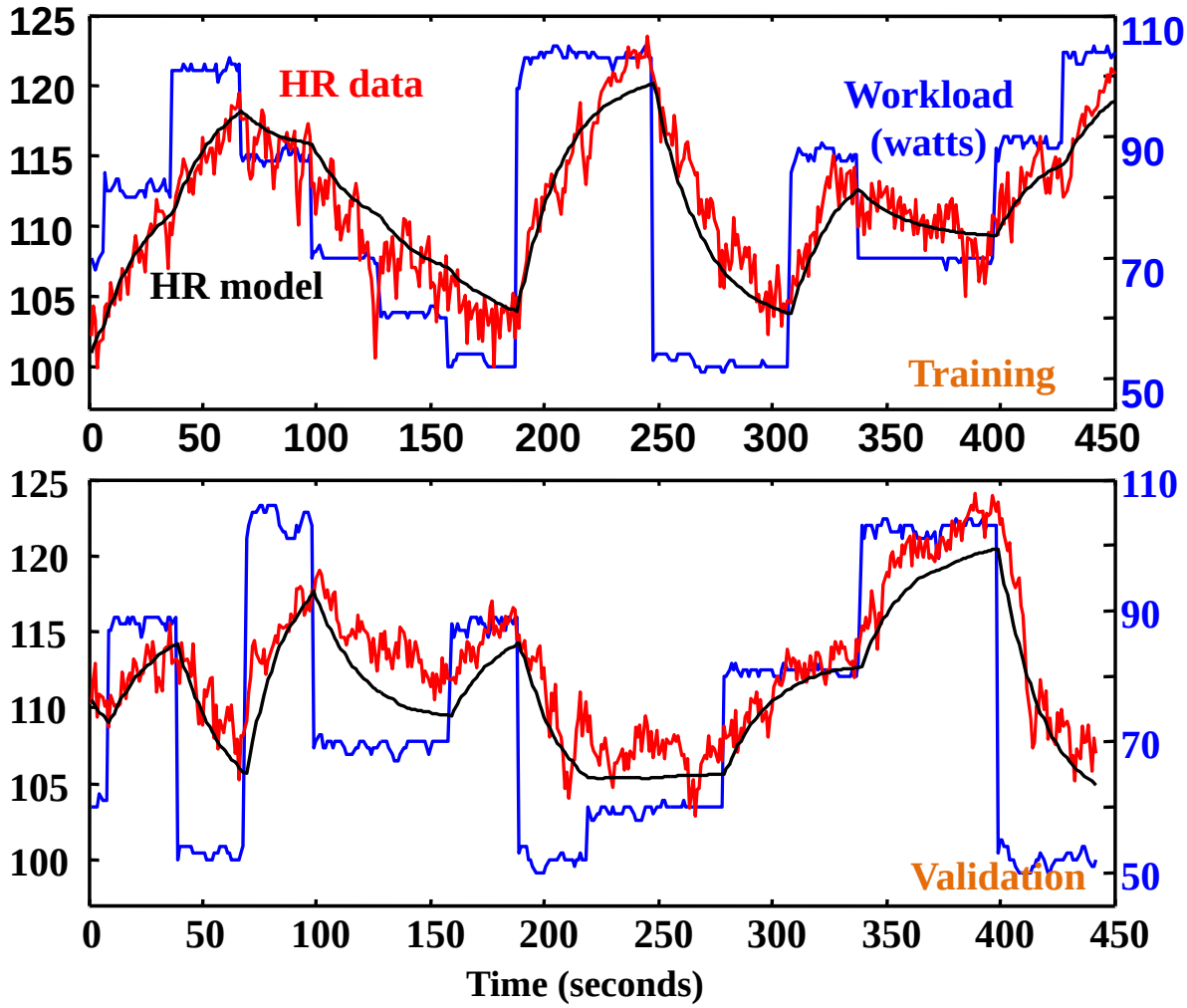

Figure S22: Subject #2 performed two separate experiments of less than 8 minutes each on a cycle ergometer including exercise levels between 50 watts and 100 watts. HR (left axis, red) is plotted for two different workload demands (right axis, blue). A 1st order linear dynamic ("black box") model (i.e., $\Delta H = aH + bW + c$) with 3 parameters (a,b,c) was fit using the upper exercise data with workload input and HR output. Simulations of this model with the 2 workload inputs are in black.

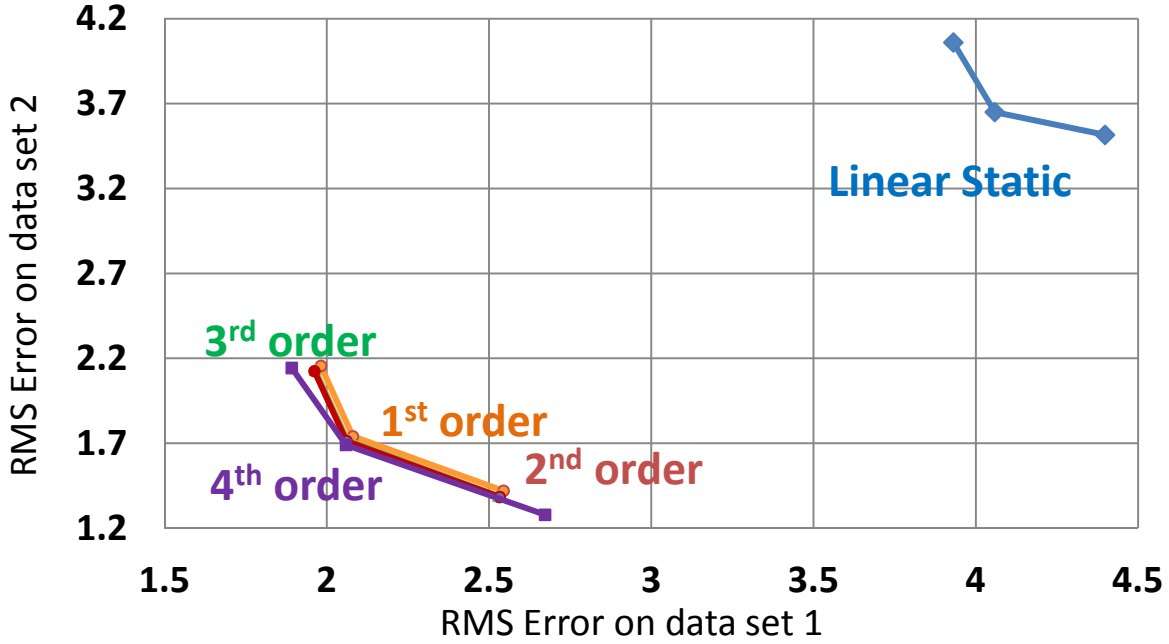

Figure S23: In this figure, we use the two experiments' data in Supplementary Figure 18 to show how validation results correlate with the complexity of the model. We call the upper experiment data set in Fig. S22 data set 1 and the lower one data set 2. The classes of models we compare in the figure are: linear static model (blue), 1st order piecewise linear models with 1 piece (orange), 2 pieces (red), 3 pieces (green), and 4 pieces (purple). For each class of models, we do three different fittings: using data set 1 to fit a model; using data set 2 to fit a model; using both data set 1 and data 2 fit a model. Then we use those models to simulate the two data sets and calculate the corresponding mean squared errors on those data sets. The mean squared error is defined as:

$$\text{error}=\sqrt{\frac{1}{N}\sum_{t=1}^{N}\left(H(t)-HR(t)\right)^2}$$

where *H(t)* and *HR(t)* are respectively the simulated and the measured heart at time point *t*, and *N* is the total number of time points. The three markers in each line for each class of models show the simulated errors using the corresponding three different fitted models, which are, from left to right, the fitted model using data set 1, the fitted model using the two data sets; the fitted model using data set 2. From this plot, we claim that 2 linear pieces are an optimal balance between model order, fit, and cross validation.

Table S1, RMS error of cross validation for linear dynamic models

	Training	Validation	Validation	Training	Fitting together	
	Data 1	Data2	Data 1	Data2	Data 1	Data2
Linear Static	3.9306	4.0603	4.3980	3.5160	4.0582	3.6503
1st order linear dynamic	1.9818	2.1553	2.5446	1.4197	2.0803	1.7402
2nd order linear dynamic	1.8200	1.4347	2.5289	1.3900	2.0631	1.7190
3rd order linear dynamic	1.8034	1.4297	2.4782	1.3815	1.8654	1.4323
4th order linear dynamic	1.8006	1.4285	2.5198	1.3487	1.7689	1.4194

2. First Principle Model

Figure S24 shows the validation result for the 1st principle model. We still use data set 1 as training data and data set 2 as validation data. The three tradeoff parameters (q_p, q_O, q_H) in the cost function of the first principle model are fitted using data set 1 (training data) with workload input and HR output. This first principle model is simulated for each data set with workload as input (blue) and HR (black) as output, which can be compared with measured HR data (red). Simulations of blood pressure (P_{as}, purple) and tissue oxygen saturation ($[O_2]_T$, green) are consistent with the literature but were not measured. . From the simulation results, we can see that the 1st principle model can predict HR response to workloads well.

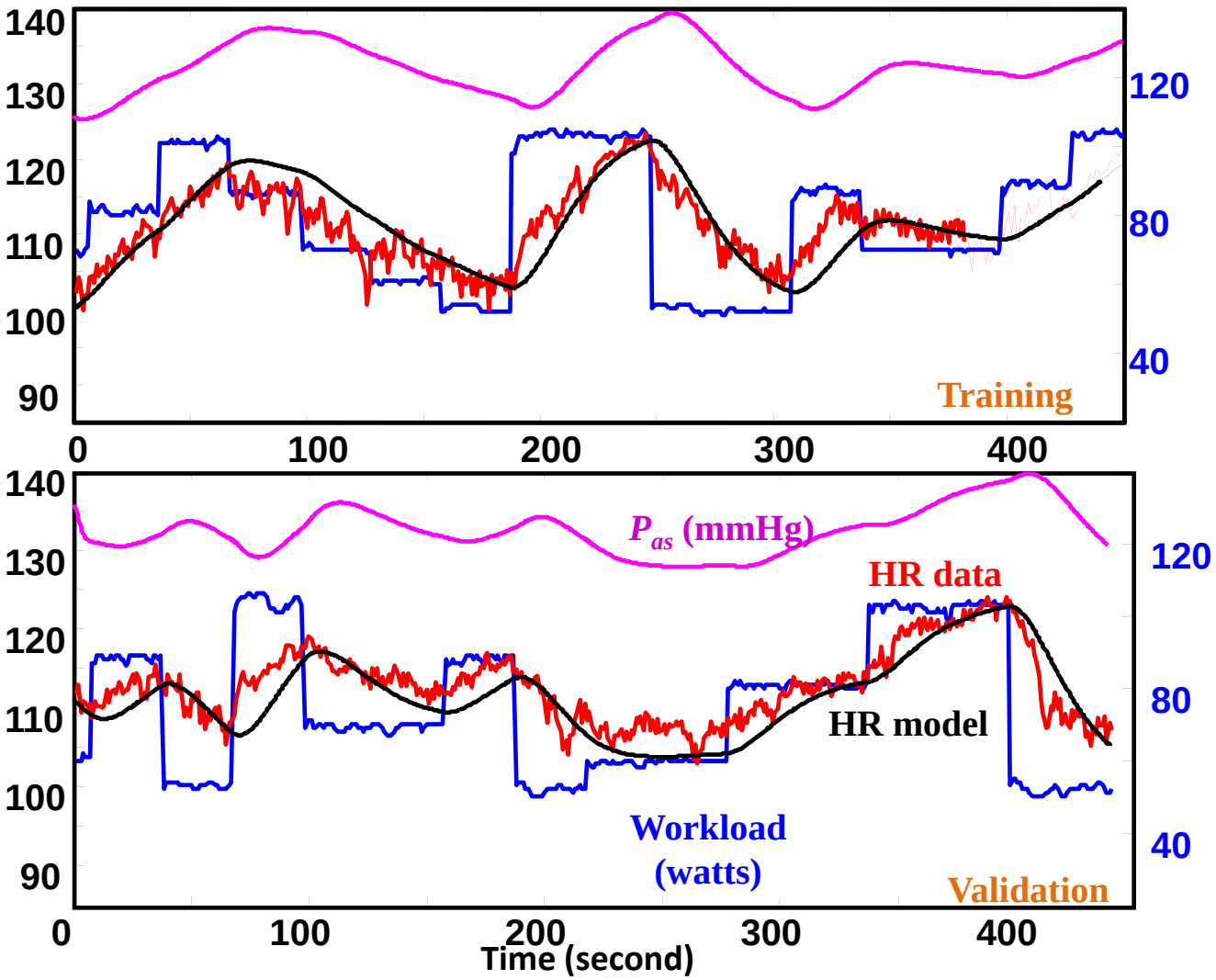

Figure S24: Subject #2's data using first principle models: optimal control model of response to the two different workload (blue) demands including exercise levels between 50 watts and 100 watts. The three tradeoff parameters in the cost function of the first principle model are fitted using the upper exercise data (i.e. training data) with workload input and HR output. This first principle model is simulated for each data set with workload as input (blue) and HR (black) as output, which can be compared with measured HR data (red). Simulations of blood pressure (P_{as}, purple) are consistent with the literature but were not measured.

3. Nonlinear System Identification Model—Piecewise Linear Dynamic Model

We carried out cross validation on the nonlinear system identification model by repeating the same process as that for the linear system identification model in SOM-Section IV-1. We call the upper data set in Figure S21 data set A and the lower data set data set B. A piecewise 1st order linear model ("black box") with 2 linear pieces and 7 parameters was fit using data set 1 with workload input and HR output and simulations of this model is done with the 2 workload as inputs. Then we fit and simulate different models with different complexities on the two data sets to study how validation results correlate with model complexities which is shown in Fig. S25-26.

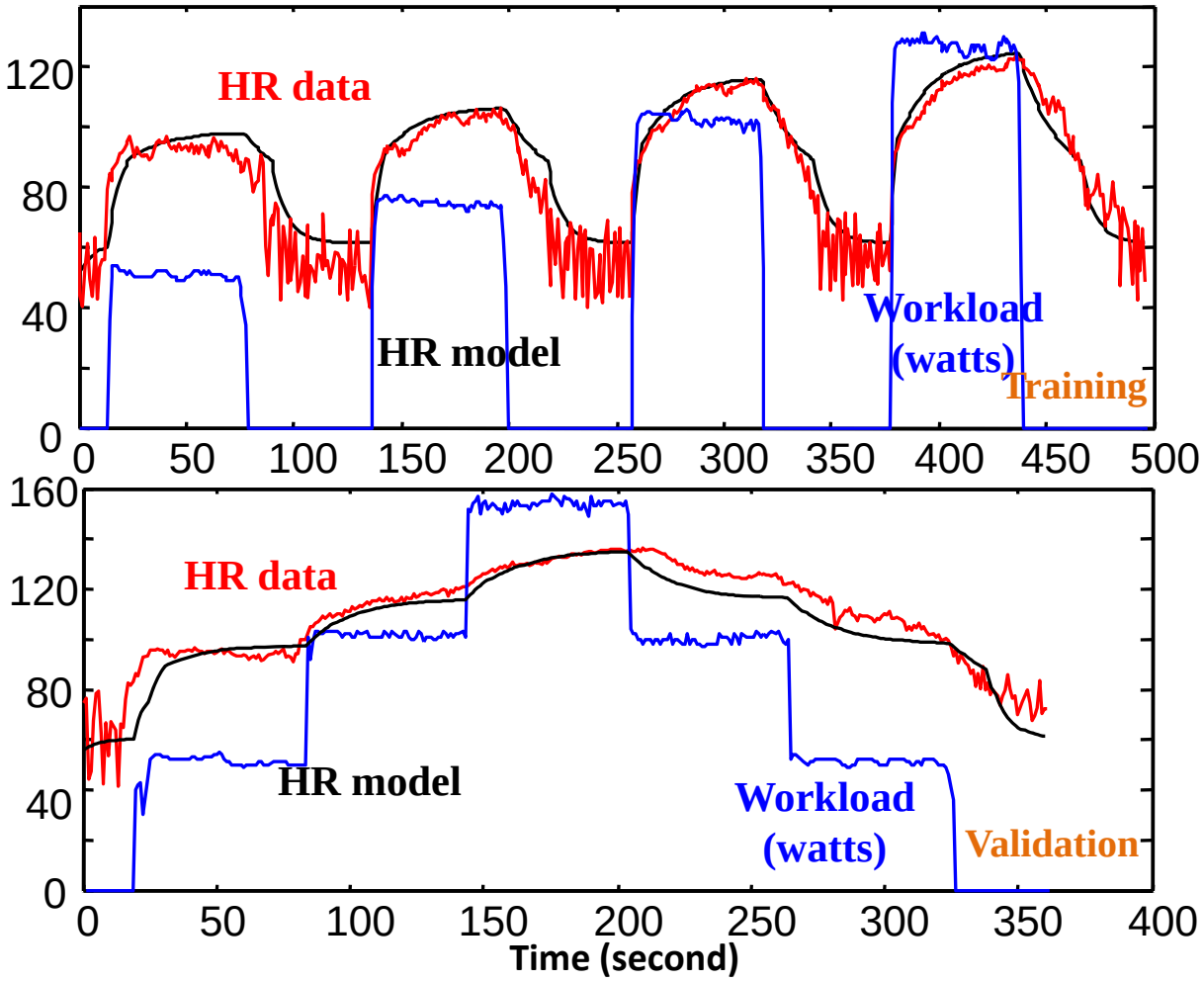

Figure S25: Validation results for the nonlinear system identification model. HR (left axis, red) is plotted for two different workload demands (right axis, blue). We use the upper data set (called as data set A) in Fig. S21 as training data and the lower data set (called as data set B) as validation data. A piecewise 1st order linear model ("black box") with 2 linear pieces and 7 parameters was fit using the training data with workload input and HR output. Simulations of this model with the 2 workload inputs are in black.

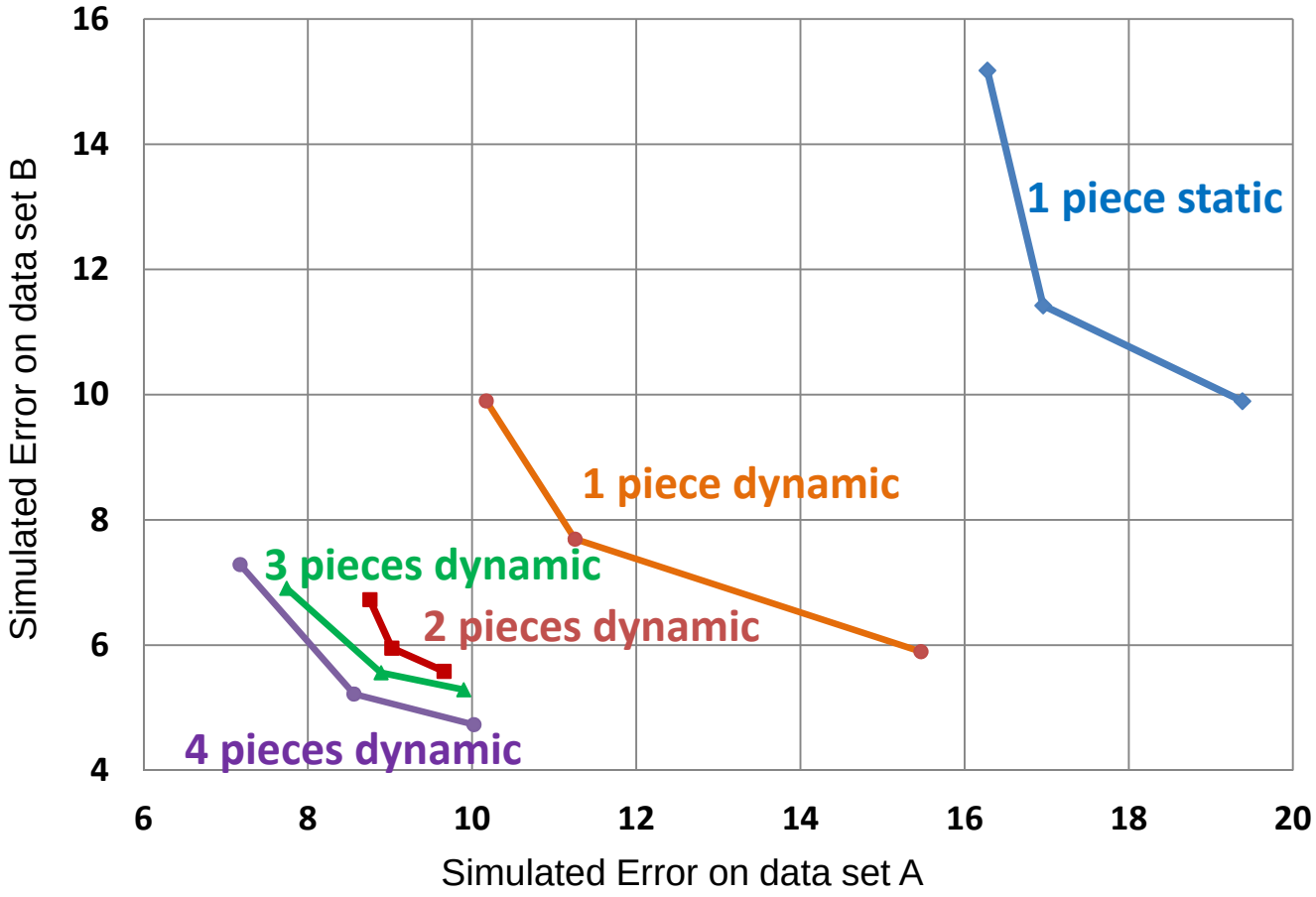

Figure S26: In this figure, we use the two experiments' data in Fig. S21 to show how validation results correlate with the complexity of the model. We call the upper experiment data set in Fig.S21 as data set A and the lower one as data set B. The classes of models we compare in the figure are: 1 piece linear static model (blue), 1st order piecewise linear models with 1 piece (orange), 2 pieces (red), 3 pieces (green), and 4 pieces (purple). For each class of models, we do three different fittings: using data set 1 to fit a model; using data set 2 to fit a model; using both data set 1 and data 2 fit a model. Then we use those models to simulate the two data sets and calculate the corresponding mean squared errors on those data sets. The mean squared error is defined as:

$$\text{error}=\sqrt{\frac{1}{N}\sum_{t=1}^{N}\left(H(t)-HR(t)\right)^2}$$

where *H(t)* and *HR(t)* are respectively the simulated and the measured heart at time point *t*, and *N* is the total number of time points. The three markers in each line for each class of models show the simulated errors using the corresponding three different fitted models, which are, from left to right, the fitted model using data set 1, the fitted model using the two data sets; the fitted model using data set 2. From this plot, we claim that 2 linear pieces are an optimal balance between model order, fit, and cross validation.

V. Tables S2-S4:

Table S2: Parameters value

Parameter	Value	Parameter	Value	Parameter	Value
c_{as}	0.01016(L/mmHg)	R_p	0.5(mmHg min/L)	V_{T,O_2}	6.0 (L)
c_{vs}	0.6500(L/mmHg)	R_{s0}	6.5(mmHg min/L)	$[O_2]_a$	0.2 (L O_2/L blood)
c_{ap}	0.0361(L/mmHg)	A	18(mmHg min /L)	ρ	0.012(L/min/watt)
c_{vp}	0.1408(L/mmHg)	V_{tot}	5.0580 (L)	M_0	0.36 (L/min)

Table S3: Parameters value for cardio output

Subject	Parameter	Value	Parameter	Value
1	c_l	0.03(L/mmHg)	c_r	0.05(L/mmHg)
2	c_l	0.025(L/mmHg)	c_r	0.045(L/mmHg)
3	c_l	0.02(L/mmHg)	c_r	0.04(L/mmHg)
4	c_l	0.032 (L/mmHg)	c_r	0.052(L/mmHg)
5	c_l	0.03 (L/mmHg)	c_r	0.05(L/mmHg)

Table S4: q value for dynamic 1st principle model

Subject		Parameter	Value	Parameter	Value	Parameter	Value
1	0-50 watts	q_{as}	30	q_{O_2}	100000	q_H	1
	100-150watts	q_{as}	65	q_{O_2}	100000	q_H	15
2	0-50 watts	q_{as}	30	q_{O_2}	100000	q_H	1
	100-150watts	q_{as}	80	q_{O_2}	100000	q_H	35
3	0-50 watts	q_{as}	40	q_{O_2}	100000	q_H	5
	50-100watts	q_{as}	65	q_{O_2}	100000	q_H	15
4	0-50 watts	q_{as}	45	q_{O_2}	100000	q_H	1
	100-150watts	q_{as}	85	q_{O_2}	100000	q_H	50
5	0-50 watts	q_{as}	40	q_{O_2}	100000	q_H	1
	100-150watts	q_{as}	80	q_{O_2}	100000	q_H	40

VI: System Identification Techniques

1 Parametric Dynamical Model

A discrete linear time invariant (LTI) system with single input single output (SISO) is applied to approximate causal dependencies between various physiological variables in our study. This LTI system is parameterized in the following obervable canonical form:

$$\begin{aligned} \Delta x[k] \triangleq x[k+1] - x[k] &= Ax[k] + Bu[k] + [0, \ldots, 0, 1]^T c \\ y[k] &= [1, 0, \ldots, 0]x[k] \qquad\qquad k = 0, 1, 2, ... \end{aligned} \tag{SI-16}$$

where A is parameterized as

$$A = \begin{bmatrix} a_1 & 1 & 0 & 0 & \cdots & 0 \\ a_2 & 0 & 1 & 0 & \cdots & 0 \\ \vdots & \vdots & \vdots & \vdots & \ddots & \vdots \\ a_n & 0 & 0 & 0 & \cdots & 0 \end{bmatrix}.$$

$x[k] \in \mathbb{R}^n$,$u[k] \in \mathbb{R}$ and $y[k] \in \mathbb{R}$ denote the state, input and output of the system, respectively. The unknowns of the system are $A \in \mathbb{R}^{n \times n}$, $B \in \mathbb{R}^n$, $c \in \mathbb{R}$ and $x[0] \in \mathbb{R}^n$, the initial condition. Given a positive discrete time instant N and two sequences of scalar data from measured physiological variables, $\hat{\boldsymbol{u}} := \{\hat{u}[k]\}_{k=0}^{N-1}$ and $\hat{\boldsymbol{y}} := \{\hat{y}[k]\}_{k=0}^{N-1}$, we estimate the unknowns of the system $(A, B, c, x[0])$ so that when $\hat{\boldsymbol{u}}$ is applied as input to the system, the resulting output, $\boldsymbol{y}$, is close to $\hat{\boldsymbol{y}}$.

The advantage of using observable canonical form is that it reduces unknown parameter dimension and thus reduces computational complexity without loss of generality. Moreover, we have observed that this form is empirically more accurate at fitting stiff systems than other state-space techniques.

2 Parameter Estimation

Denote $E_c = [0, \ldots, 0, 1]^T$ and $E_r = [1, 0, \ldots, 0]$. Using the parameterization given above, the solution to (SI-16) for a given input signal $\hat{\boldsymbol{u}}$ is

$$y[k] = E_r A^{k-1} x[0] + \sum_{i=1}^{k-1} E_r A^{k-1-i} B u(i) + \sum_{i=1}^{k-1} E_r A^{k-1-i} E_c c$$

for $k = 0, 1, 2, \ldots, N-1$. The parameter estimation problem can then be stated as follows. For fixed n, we wish to find A, B, c and $x[0]$ that minimize the mean squared error between $\boldsymbol{y}$ and $\hat{\boldsymbol{y}}$, i.e. we wish to minimize

$$V\left(A, B, c, x[0]\right) = \frac{1}{N} \sum_{k=0}^{N-1} \frac{1}{2} \left[\hat{y}[k] - y[k]\right]^2.$$

Letting $\varphi_A[k] = \begin{bmatrix} E_r A^{k-1} & \sum_{i=1}^{k-1} u(i) E_r A^{k-1-i} & \sum_{i=1}^{k-1} E_r A^{k-1-i} E_c \end{bmatrix}$ and $\xi = \begin{bmatrix} x[0]^T & B^T & c \end{bmatrix}^T$, the solution to (SI-16) can be rewritten as $y[k] = \varphi_A^T[k]\xi$, and the quadratic cost criterion becomes

$$V\left(A, \xi\right) = \frac{1}{N} \sum_{k=0}^{N-1} \frac{1}{2} \left[\hat{y}[k] - \varphi_A^T[k]\xi\right]^2.$$

From this it is clear that if $\varphi_A[k]$ is known for $k = 0, \ldots, N-1$, minimizing V with respect to ξ is a linear least-squares problem that has a unique global minimum and can be solved efficiently. Since $\boldsymbol{\varphi_A}$ only depends on A, for fixed A, $\varphi_A[k]$ can be computed for $k = 0, \ldots, N-1$. Thus, our approach to the parameter estimation problem is to employ a direct search over the space parameterizing A, wherein the cost associated with a point A_0 is $\min_{\xi} V(A_0, \xi)$. Since A is parameterized in observable canonical form, the direct search occurs over an n-dimensional space. Letting $\hat{Y} = \begin{bmatrix} \hat{y}[0] & \hat{y}[1] & \cdots & \hat{y}[N-1] \end{bmatrix}^T$ and $\Phi_A = \begin{bmatrix} \varphi_A[0] & \varphi_A[1] & \cdots & \varphi_A[N-1] \end{bmatrix}^T$ we have that, for fixed A,

$$\left(\Phi_A^T \Phi_A\right)^{-1} \Phi_A^T \hat{Y} = \arg\min_{\xi} V(A, \xi). \tag{SI-17}$$

Thus, the cost criterion used in the direct search for A can be written as

$$\overline{V}(A) = \frac{1}{N} \sum_{k=0}^{N-1} \frac{1}{2} \left[\hat{y}[k] - \varphi_A^T[k] \left(\Phi_A^T \Phi_A\right)^{-1} \Phi_A^T \hat{Y}\right]^2.$$

We use the Nelder-Mead simplex algorithm as our direct search method for estimating A. This is a nonlinear unconstrained optimization algorithm that attempts to minimize scalar-valued nonlinear functions using only function values, i.e. without gradient information. Because the objective $V(A)$ is nonconvex, we cannot guarantee that our estimate for A is globally optimal. Nonetheless, A is parametrized by relatively few variables, and our direct search is thus restricted to a low-dimensional space. We therefore expect that our method of eliminating parameters $(B, c, x[0])$ and then searching only for A provides a more optimal estimate than would be obtained via a joint optimization over $(A, B, c, x[0])$. Though the Nelder-Mead algorithm is not guaranteed to find the globally optimal A, we observe in practice that this direct search is insensitive to our initial search point. We suspect this is because we focus on 1st and 2nd oder LTI models, and the search space for A is consequently very low dimensional.